

Investigation of Methods to Produce Regional Maps of Liquefaction-Induced Deformation: A Pilot Study

K. L. Knudsen¹, A. Rosinski¹, M.O. Wieggers¹, C.R. Real², J. Wu³, R. B. Seed⁴,

¹California Geological Survey, San Francisco, CA

²California Geological Survey, Sacramento, CA

³URS Corporation, Oakland, CA

⁴Dept. of Civil and Environmental Engineering, Univ. of California at Berkeley

EXECUTIVE SUMMARY

Regional maps of liquefaction hazards typically are based on the susceptibility of materials to liquefaction, or the likelihood that a liquefaction-triggering threshold will be exceeded. This report describes a project to assess the feasibility of producing regional (1:24,000-scale) liquefaction hazard maps that are based on magnitudes of potential liquefaction-induced deformation. The study area is the central Santa Clara Valley, at the south end of San Francisco Bay in Central California. The information collected and used includes: a) 1:24,000-scale Quaternary geological mapping, b) over 650 geotechnical borings, c) 4 types of digital terrain information, d) probabilistic earthquake shaking information, and e) regional maps of historical high ground-water levels.

Some of the parameters used to evaluate liquefaction hazard (e.g. penetration resistance and sediment texture) exhibit wide variability over short distances, even within individual geologic map unit polygons. Point data (borings) and cross sections developed using the borings may not sufficiently depict this variability. Geotechnical boring data is used to: (a) develop contour maps or isopach maps of the paleotopography showing thickness of Holocene deposits and the proportion of this sediment stack that is likely to liquefy and deform under earthquake shaking; and (b) assess the variability in engineering properties within and between geologic map units. One of the decisions to be made is how to relate the sediment depicted on boring logs and the geotechnical properties of these materials, to geologic map units. One can simply relate the material properties observed on the boring log to the geologic unit mapped at the surface where a boring is advanced, or once can assign a "representative deposit age" for each boring, or an age and environment of deposition can be assigned to every layer in every boring. Each of these approaches has been taken in this study.

There are two classes of available methods for predicting liquefaction-induced deformation magnitudes, both of which are typically used in site investigations, not in regional mapping. These method classes are empirical predictions of lateral spread (horizontal) displacements, and predictions of volumetric and shear strains. Predictions of strain can be made using either semi-empirical formulations or numerical simulations. In this pilot project, methods of predicting lateral spread displacements are investigated and employed and a variety of sources and types of digital terrain information are evaluated. Empirical relations to estimate future volumetric and shear strain are assessed

and used. Liquefaction potential index was calculated for all borings and the calculated values were related to the geologic map unit shown on surficial Quaternary geologic maps.

The most interesting and challenging aspect of producing liquefaction deformation maps is relating the deformation magnitudes that are calculated for each geotechnical boring to some form of two-dimensional hazard map. Attempts were made to contour the point data (estimates of settlement, horizontal displacement, thickness of sediment with liquefiable textures, T_{15} , and LPI), but the highly variable nature of the deposits in the study area made this difficult. Preliminary geostatistical analysis shows that a much greater density of boring data (perhaps double the more than 650 borings that were available for this project) is needed to adequately characterize the highly variable geology in this study area.

Lateral spread estimates and maps were developed using a four-parameter empirical model. The seismic parameters for this model (from the state's probabilistic shaking hazard maps) can be resolved to a grid cell resolution of no finer than 1 km^2 , according to the producers of these maps. Four types of terrain information were evaluated for their usefulness in characterizing gently sloping ground surfaces and "free face ratio", a ratio of the height of a free face to the distance from that free face. Photogrametric break lines best depict free faces and the readily available USGS 10-m DEM best depict gently sloping ground surfaces. "Bald earth" DEMS produced using LiDAR and Interferometric Radar were not particularly useful in this exercise. The final parameter, T_{15} , or thickness of saturated sediment of liquefiable texture with blow counts less than 15, was found to be difficult to model in Santa Clara Valley with the density of geotechnical boring data available for this project.

The results of this feasibility study suggest that strain-based methods that incorporate topographic parameters like slope and free face ratio are the most promising avenue for additional research. A significant hurdle with any regional mapping effort will be to resolve the issues arising from highly variable geology and variability of parameters within map units being as large as the variability between map units. We are continuing to work at developing statistically valid ways of characterizing natural deposits that will be useful in regional hazard mapping.

ACKNOWLEDGMENTS

This project was sponsored in part by the University of California at Berkeley's Pacific Earthquake Engineering Research Center's Program of Applied Earthquake Engineering Research of Lifeline Systems supported by the State Energy Resources Conservation and Development Commission and the Pacific Gas & Electric Company. The financial support of the PEARL sponsor organizations including Pacific Gas & Electric Company, the California Energy Commission, and the California Department of transportation is acknowledged. This work made use of the Earthquake Engineering Research Center's Shared Facilities supported by the National Science Foundation under Award #EEC-9701568. The authors wish to thank Cliff Roblee, Michael Riemer and Tom Shantz for their guidance and support. A number of California Geological Survey personnel have provided support, including Teri McGuire, Marvin Woods, Kevin Clahan and Jackie Bott. Carl Wentworth (U.S. Geological Survey) and Christopher Hitchcock and Edward Helley also collaborated on geological interpretation of deposits in Santa Clara Valley. Geotechnical borings were obtained from a variety of organizations and jurisdictions, including: Santa Clara Valley Water District, City of San Jose, City of Milpitas, URS Corporation, William Lettis & Associates, and CALTRANS.

Keywords—**deformation, displacement, ground failure, lateral spread, liquefaction, seismic hazard, settlement**

TABLE OF CONTENTS

- Executive Summary
- Acknowledgments
- Table of Contents
- List of Figures
- List of Tables
- Introduction
- Study area and setting
 - Physiography
 - Geologic and geomorphic setting
 - Seismicity and ground motions
 - Subsidence
 - Past earthquake-induced liquefaction and ground failures in the study area
- Methods
 - Geologic and geotechnical characterization
 - Liquefaction assessments
 - Predictions of volumetric and shear strain
 - Lateral spread predictions
 - Liquefaction potential index approach
- Results
 - Properties of study area sediment – Descriptive statistics
 - Estimating strain for each geologic map unit
 - Prediction of lateral spread deformation
 - Liquefaction potential index approach
- Conclusions and recommendations
- References

LIST OF FIGURES

- Figure 1. Southern San Francisco Bay Area, 7.5-minute topographic quadrangles, and zones of required investigation for liquefaction and earthquake-induced landsliding
- Figure 2. Quaternary geologic map of the Milpitas 7.5-minute quadrangle (from Knudsen et al., 2000)
- Figure 3. Geologic map unit correlation chart to accompany Quaternary geologic map of Knudsen et al. (2000)
- Figure 4. Image showing the San Francisco Bay Area and its principal faults (red lines)
- Figure 5. Historic ground failure in the northern Santa Clara Valley (modified from Knudsen et al., 2000)
- Figure 6. Methods employed during this feasibility study. Boxes that are dashed indicate points in the process where characterizing geologic and measurement variability is important
- Figure 7. Geotechnical boring log and relating layers and borings to geologic map units.
- Figure 8. Pleistocene surface elevation (ft), after Clahan and others (2002)
- Figure 9. Methods of predicting liquefaction-induced deformation
- Figure 10. Tokimatsu and Seed (1984) method of predicting volumetric strain and limiting shear strain (from Tokimatsu and Seed, 1984)
- Figure 11. Ishihara and Yoshimine (1992) method for predicting volumetric and shear strain (from Ishihara and Yoshimine, 1992)
- Figure 12. Shamoto et al. (1998) chart showing the interdependency of volumetric and shear strains for different levels of irreversible dilatancy (from Shamoto et al., 1998)
- Figure 13. Shamoto et al. (1998) relationships used to predict residual volumetric and shear strain (from Shamoto et al., 1998)
- Figure 14. Proposed correlations between CSR, $(N_1)_{60,cs}$ and reconsolidation volumetric strain (from Wu et al., 2004)
- Figure 15. Proposed correlations between CSR, $(N_1)_{60,cs}$ and limiting shear strain (from Wu, 2002)
- Figure 16. Defining ground slope (S) and free face ratio (W), from Bartlett and Youd, 1992)
- Figure 17. Parameter sensitivity analysis, four and six parameter lateral spread models, for sloping ground (GS) and free face (FF) conditions.
- Figure 18. Histograms showing fines corrected penetration resistance $[(N_1)_{60,cs}]$ for each geologic map unit
- Figure 19. “Box and whisker” plot showing fines corrected penetration resistance values $[(N_1)_{60,cs}]$ for all geologic map units
- Figure 20. Histograms showing aggregate penetration resistance $[(N_1)_{60,cs}]$ for artificial fill, Holocene and Late Pleistocene layers
- Figure 21. Liquefaction-induced vertical strain, Milpitas 7.5-minute Quadrangle, California (strain calculated using Wu et al., 2004 method)
- Figure 22. Liquefaction-induced ground settlement (ft), Milpitas 7.5-minute Quadrangle, California (settlement calculated using Wu et al., 2004 method)

- Figure 23. Lateral spread study area showing free face and sloping ground areas. Shaded relief image generated from photogrammetric breaklines and elevation points generated for orthophotographic rectification.
- Figure 24. Shaded relief image from USGS DEM showing poor depiction of free face along the bank of the Guadalupe
- Figure 25. Shaded relief image made from photogrammetric breaklines and elevation points showing accurate depiction free faces along Coyote Creek and Guadalupe River
- Figure 26. Shaded relief from bald earth interferometric radar data
- Figure 27. Shaded relief image from bald earth interferometric radar DEM showing false undulations in topography and poor depiction of free faces along bank of Guadalupe River
- Figure 28. Moment magnitude grid
- Figure 29. Slope gradient grid
- Figure 30. Free face ratio grid
- Figure 31. T_{15} grid
- Figure 32. Semivariogram for T_{15} parameter
- Figure 33. Horizontal displacement grid for areas analyzed for gentle slope conditions.
- Figure 34. Horizontal displacement grid for areas analyzed for free face conditions.
- Figure 35. Liquefaction potential index calculated for borings aggregated to three ages of deposits: Artificial fill, Holocene and Late Pleistocene

LIST OF TABLES

- Table 1. Quaternary geologic map units (modified from Knudsen et al., 2000)
- Table 2. Fines content (FC) assigned to samples for which no textural data was provided on boring logs
- Table 3. Calculation of strain parameters and the methods used to calculate them in this project
- Table 4. Percentage of each geologic map unit with textures that are potentially liquefiable
- Table 5. Fines corrected penetration resistance, factor of safety, and cyclic resistance ratio for all geologic map units
- Table 6. Calculation of volumetric and limiting shear strain, along with settlement and horizontal displacement for each geologic map unit
- Table 7. Summary of geologic map unit groupings for T₁₅
- Table 8. Summary of horizontal displacement in the part of the study area that was analyzed for gentle slope conditions
- Table 9. Summary of horizontal displacement in the part of the study area that was analyzed for free face conditions
- Table 10. LPI values for geologic map units

INTRODUCTION

Most liquefaction hazard maps are based on an evaluation of the likelihood that materials will liquefy, or that liquefaction will be “triggered”, during future earthquakes.

Typically, categories of very high to low or very low are assigned to each Quaternary geologic map polygon, with deviations from a one-to-one correspondence between Quaternary map unit and liquefaction susceptibility category based on differences across the region in depth to ground water and expected levels of earthquake ground shaking. This approach is based solely on whether soil/sediment can be expected to liquefy, not on the consequences of that liquefaction or on how much ground surface deformation might accompany the triggering of liquefaction.

This report presents the results of an investigation into the feasibility of producing regional (1:24,000-scale) hazard maps that are based on predicted surface deformation resulting from liquefaction. Liquefaction induced-deformation maps would be better suited to emergency response planning, mitigation prioritization and lifeline system vulnerability assessments than the classical liquefaction susceptibility or liquefaction potential maps. Deformation-based maps may in the future serve as the basis for the California Geological Survey’s liquefaction zones of required investigation.

Most previous efforts to map potential liquefaction-induced deformation on a regional scale have been based on predictions of lateral spread displacements (e.g. Youd et al., 1993). Any attempt to produce maps of future liquefaction-induced deformation must take into account the nature and variability of geologic deposits in the area to be mapped. This task is complicated by the limited subsurface data (geotechnical boring logs) that are generally available in most areas. In this study, about 650 boring logs are used to characterize the geology of the Northern Santa Clara Valley, which is an area with considerable variability in its late Pleistocene and Holocene deposits. Because maps, in this case liquefaction hazard maps, are inherently two-dimensional, most liquefaction hazard maps are really derivative Quaternary geologic maps. Researchers have used a variety of hazard assessment techniques to assign a degree of hazard to each Quaternary map unit polygon that has been mapped in their area of interest. The crux of the problem investigated here is to devise a way to relate the highly variable results of analysis of geotechnical borings to two dimensional hazard maps.

This study consisted of several tasks:

- 1) A review of existing methods for predicting deformation caused by liquefaction
- 2) Characterization of the study area and setting using geologic maps, available subsurface geotechnical data, existing ground motion maps and existing information on historical high ground-water levels
- 3) Statistical treatment of aggregate (geotechnical boring) data to identify parameters that can be used to characterize sediment/soils depicted in boring logs
- 4) Calculation of liquefaction-induced volumetric and shear strains
- 5) A comparative evaluation of available digital terrain data for use in empirical lateral spread calculations.

- 6) A lateral spread analysis using a four-parameter empirical model developed by Bardet and others (1999). Input grid files were developed for each of the model parameters and output grid files of estimated ground displacement were produced.
- 7) Calculation of Liquefaction Potential Index (LPI) values for all borings and evaluation of their suitability for making regional hazard maps.
- 8) Development of maps using results of the volumetric and shear strain calculations.
- 9) Production of this report documenting what was learned in this pilot project.

STUDY AREA AND SETTING

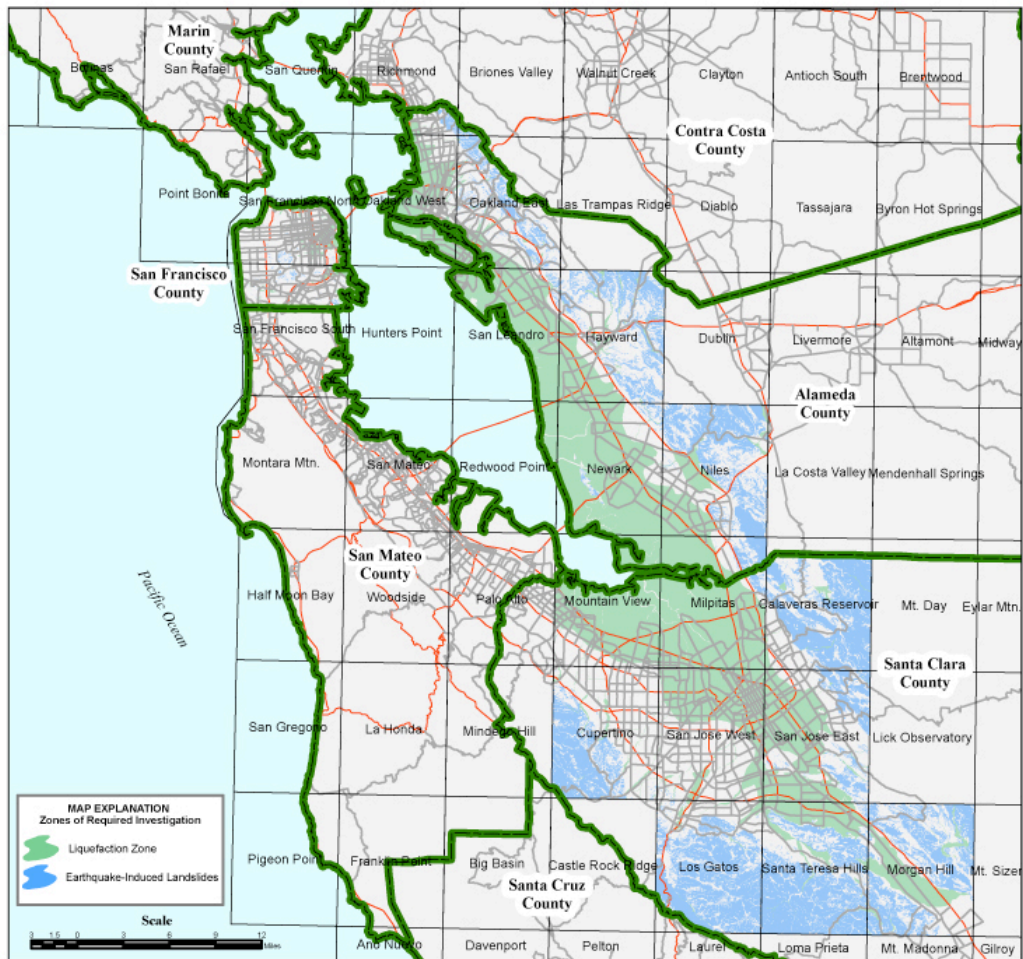
The study area chosen for this project is the Northern Santa Clara Valley. It was chosen because the CGS Seismic Hazards Mapping Program (several members of this project team work in this program) has previously developed liquefaction zone of required investigation maps for this area.

Physiography

The study area, located in the southern San Francisco Bay region of northern California, covers approximately 390 square kilometers of northern Santa Clara Valley. It covers portions of the Milpitas, Calaveras Reservoir, San Jose East, and San Jose West 7.5-minute quadrangles (Figure 1). The majority of the study area is heavily urbanized. The city of San Jose covers a large percentage of northern Santa Clara Valley, however, parts of the cities of Alviso, Campbell, Los Gatos, Milpitas, Santa Clara, Saratoga, and Sunnyvale, are also included.

The northern end of the study area, along the margin of San Francisco Bay, is occupied by salt evaporation ponds and associated constructed levees. The San Jose International Airport is located in the north-central part of the study area. Numerous streams cross the northern Santa Clara Valley. The two largest systems are Guadalupe River and Coyote Creek. Guadalupe River is fed by Saratoga, San Tomas Aquinas, Calabazas and Los Gatos creeks, all of which originate in the Santa Cruz mountains to the west. Coyote Creek is fed by Berryessa, Penitencia, Tualcritos, Scott, Arroyo de los Coches, Piedmont, Calara, Miguelita, Silver, Babb and Thompson creeks, all of which originate in the Diablo Range to the east.

There are six major freeways that cross the study area. Northwesterly trending U.S. Highway 101 (Bayshore Freeway) connects the northern Santa Clara Valley to the San Francisco Peninsula, and northeasterly trending Interstate 680 closely parallels the foothills of the Diablo Range and connects the northern Santa Clara Valley to major cities along the east side of San Francisco Bay. State Highway 17/ Interstate 880 extends southward in the western part of the study area. Trending roughly east-west, State Highway 237 and Interstate 280 cross the northern part of the study area.



Seismic Hazard Zonation of Northern California

April 2004

Figure 1. Southern San Francisco Bay Area, 7.5-minute topographic quadrangles, and zones of required investigation for liquefaction and earthquake-induced landsliding. The study area for this project includes the Milpitas, Calaveras Reservoir, San Jose West and San Jose East quadrangles.

Geologic and Geomorphic Setting

The northwest-trending northern Santa Clara Valley, part of the Coast Range geomorphic province, is situated between the Santa Cruz mountains to the west, and the Diablo Range to the east. The northern Santa Clara Valley area recently has been mapped at 1:24,000 scale by Knudsen et al. (2000) and J.M. Sowers of William Lettis & Associates, Inc. (unpublished). An example of this mapping is shown in Figure 2, a map of the Quaternary geology of the Milpitas 7.5-minute quadrangle. The list of geologic map units shown on these maps is sorted by age in Table 1 and the map unit correlation chart is presented in Figure 3. In the northern Santa Clara Valley Knudsen et al. (2000) show 23 Quaternary map units. Much of the densely populated part of the Santa Clara Valley rests on broad alluvial fans deposited by Coyote Creek and the Guadalupe River that slope gently northwestward toward San Francisco Bay. Along the west and southwest

sides of the valley, at the base of the Santa Cruz mountains, Pleistocene alluvial fans (Qpf) are overlain by thin deposits of Holocene alluvial fan deposits (Qhf) (Knudsen et al., 2000). Along the east and northeast side of the valley, at the base of the Diablo Range, Pleistocene (Qpf) and Holocene alluvial fans (Qhf) are smaller than fans on the west side of the valley, and only minor levees (Qhl) have developed. Holocene alluvial fans generally are composed of a poorly sorted mixtures of gravel, sand, silt, and clay. At the upstream end of the alluvial fans, where gradients are steeper, fan deposits typically are composed of coarser grained material (Qhf), and grade into finer grained material (Qhff) downstream. Where the fans terminate at the edge of San Francisco Bay, fine grained material transitions into Holocene fine-grained alluvial fan-estuarine complex deposits (Qhfe), Holocene San Francisco Bay Mud (Qhbm) and Artificial fill over Bay Mud (afbm). Down the northwest-trending axis of the valley, both Guadalupe River and Coyote Creek contain Holocene stream channel deposits (Qhc), and artificial channel (ac) deposits, and are flanked by Holocene alluvial fan levee deposits (Qhl) and Holocene terrace deposits (Qht) (Figure 2). Artificial fill (af) primarily consists of linear bodies associated with large-scale transportation infrastructure, including highways and railroads, such as the interchange for U.S. Route 101 with Interstate Routes 280 and 680 near the center of the study area.

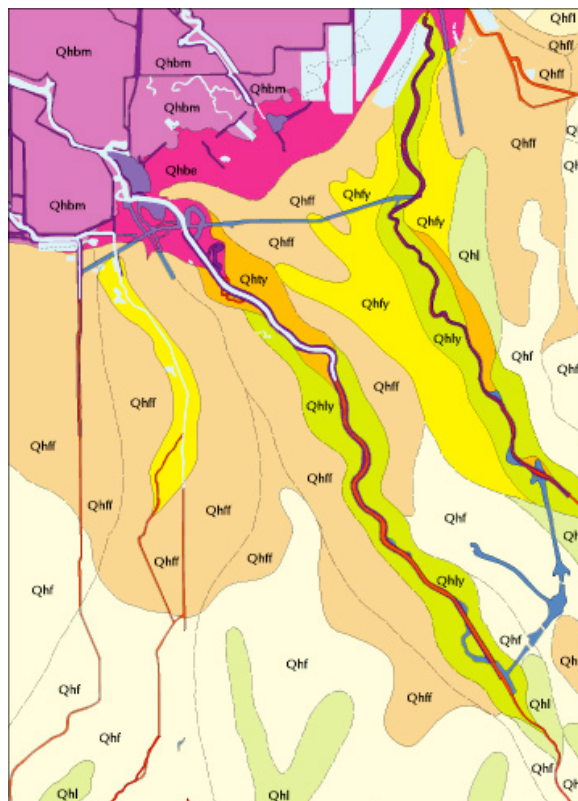


Figure 2. Quaternary geologic map of the Milpitas 7.5-minute quadrangle (from Knudsen et al., 2000)

TABLE 1. QUATERNARY GEOLOGIC MAP UNITS (modified from Knudsen et al., 2000)

Environment of deposition		Environment of deposition	
Modern			
af	Artificial fill	gq	Gravel quarry
afbm	Artificial fill over Bay Mud	ac	Artificial stream channel
alf	Artificial fill, levee	Qhc	Modern stream channel
Latest Holocene			
Qhfy	Alluvial fan	Qhty	Stream terrace
Qhly	Alluvial fan levee		
Holocene			
Qhbm	San Francisco Bay mud	Qhff	Alluvial fan, fine facies
Qhb	Basin	Qhl	Alluvial fan levee deposits
Qhfe	Fine grained alluvial fan-estuarine complex	Qht	Stream terrace
Qhf	Alluvial fan	Qha	Alluvium, undifferentiated
Latest Pleistocene to Holocene			
Qf	Alluvial fan	Qt	Stream terrace
Ql	Alluvial fan levee	Qa	Alluvium, undifferentiated
Latest Pleistocene			
Qpb	Basin	Qpa	Alluvium, undifferentiated
Qpf	Alluvial fan		
Early to late Pleistocene			
Qof	Alluvial fan	Qoa	Alluvium, undifferentiated
Pre-Quaternary			
br	Bedrock		

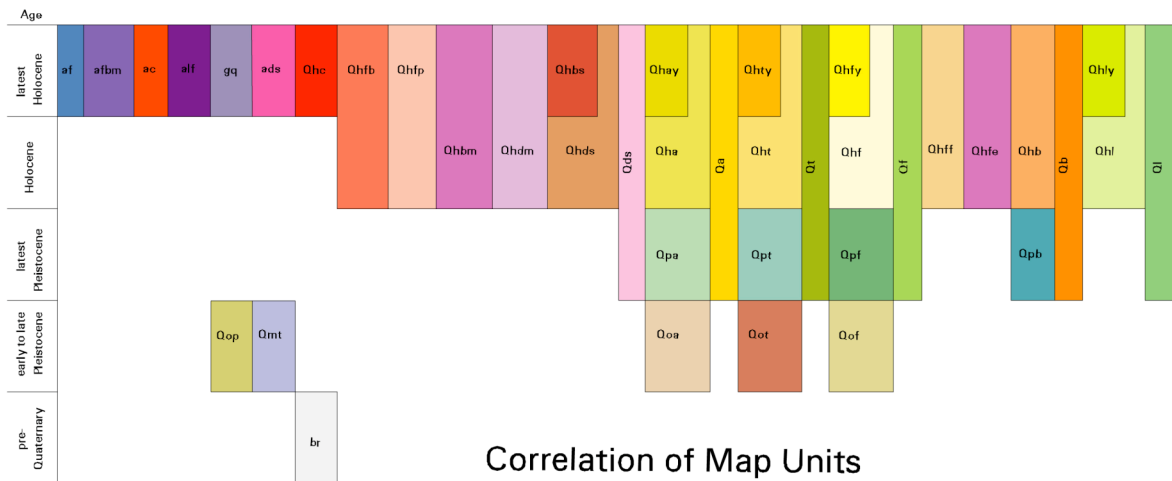


Figure 3. Geologic map unit correlation chart to accompany Quaternary geologic map of Knudsen et al. (2000)

Bedrock geology in the vicinity of the study area is divided into individual fault-bounded structural blocks based on differing stratigraphic sequences and geologic histories (Wentworth and others, 1999). Rocks from the Silver Creek, Alum Rock and Mt. Hamilton blocks are found within the four quadrangles included in the study area. At the southeastern end of the study area, rocks of the Franciscan Complex (fm) are juxtaposed against Jurassic rocks of the Coast Range Ophiolite (Jsp) along a low-angle thrust fault in

the Silver Creek structural block (Wentworth and others, 1999). Rocks of the Silver Creek block are found in the Silver Creek watershed and in the vicinity of Yerba Buena ridge. The Alum Rock block is composed of Jurassic to Quaternary age rocks and is mapped along the eastern margin of the northern Santa Clara Valley. The Alum Rock block is separated from both the Silver Creek block to the south and the Mt. Hamilton block to the east by the Calaveras Fault. Cretaceous and Jurassic rocks of the Eastern Belt, Franciscan Complex are exposed in the northeastern part of the study area.

Seismicity and Ground Motions

The northern Santa Clara Valley is bounded on the west by the San Andreas Fault system, and on the east by the Calaveras and the southern end of the Hayward Fault systems (Figure 4). Among the most significant historic earthquakes in the region are the magnitude M7.0 Hayward earthquake of October 21, 1886, the M7.9 San Francisco earthquake of April 18, 1906, and the magnitude M_w 6.9 Loma Prieta earthquake of October 17, 1989. Each of these earthquakes caused ground failure(s) in the northern Santa Clara Valley.



Figure 4. Image showing the San Francisco Bay Area and its principal faults (red lines). The approximate boundaries of the study area are shown by the blue rectangle. Map image from the USGS.

The level of seismic excitation used for this study is the level of peak ground acceleration (PGA) with a 10% probability of exceedance over a 50-year period (CGS, 2000). The statewide probabilistic seismic hazard analysis (Peterson and others, 1996) indicates that peak ground accelerations with a 10% probability of exceedance in 50 years are expected to range from about 0.5g near the margin of San Francisco Bay to about 0.8g in the foothills of the Diablo Range at the northeast corner of the study area (CGS, 2001). Deaggregation of the seismic hazard model yields the magnitude and distance of the earthquake that contributes most to the probabilistic ground motion estimate at a particular location. The deaggregation indicates that the seismic hazard in the southwest part of the study area is dominated by a M_w 7.9 earthquake on the San Andreas Fault at a distance ranging from about 18 km to 24 km. The seismic hazard in the northeast part of the study area is dominated by a M_w 7.1 earthquake on the Hayward Fault at a distance

ranging from about 2km to 7 km. The southeast part of the map area is dominated by an $M_w6.4$ earthquake on the southeast extension of the Hayward Fault at a distance of about 7 km.

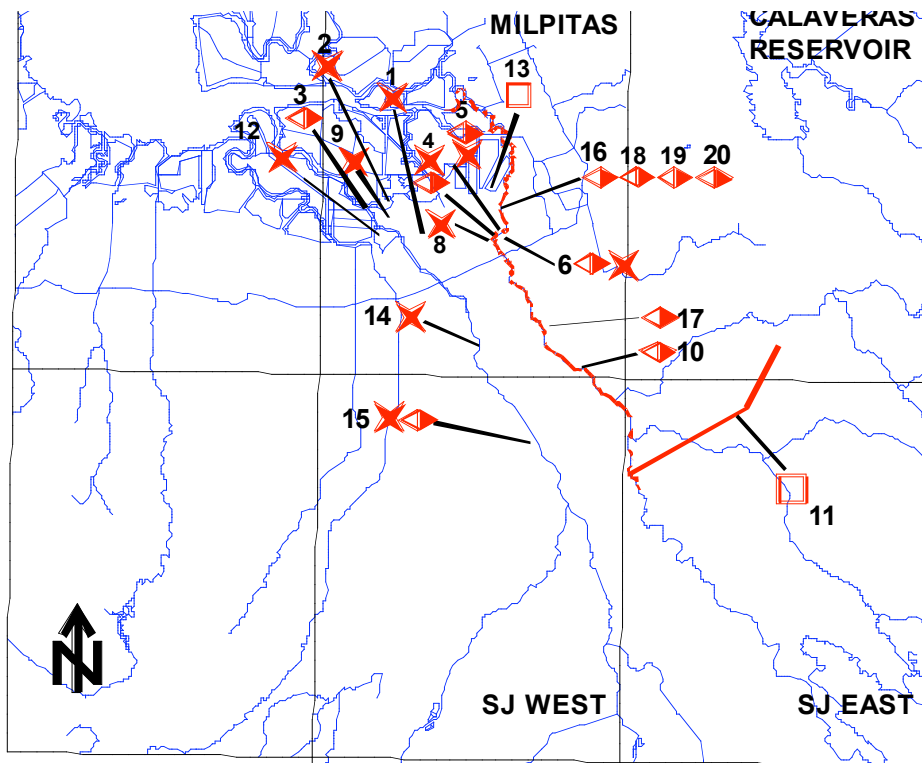
Subsidence

Subsidence due to ground-water withdrawal is well documented in the northern Santa Clara Valley. The alluvial fill in the northern Santa Clara Valley primarily consists of Pliocene to Holocene deposits, with sand and gravel more prevalent on alluvial fans along the valley margins, transitioning to silt and clay towards the San Francisco Bay (Poland, 1984). In the early part of the last century, ground-water withdrawal was primarily for agricultural use, however, by the middle of the last century agricultural water use declined while urban/municipal water use increased (Poland, 1971). Most of the subsidence in the northern Santa Clara Valley was accommodated by compaction of fine-grained sediment caused by withdrawal of ground water from confined and semi-confined aquifers (Ingebritsen and Jones, 1999).

Between approximately 1915 and 1967, as much as 2.4 meters of subsidence occurred, and overall, a region of approximately 260 km² subsided more than one meter (Poland, 1984). Careful monitoring and management of the basin, including importation of surface water, has led to the recovery of some of the subsidence. The Santa Clara Valley Water District recently has observed an increasing number of artesian wells, which reflects rising ground-water levels (Seena Hoose, SCVWD, personal communication, 2000). Within the study area, historical depths to ground water range from less than several meters near the San Francisco Bay to 10-25 meters. As ground-water levels rise, vertical effective stress is reduced, causing regional uplift (Schmidt and Bürgmann, 2002). InSAR time-series data record net uplift in the study area averaging approximately 15-20 mm between 1992 and 1998, with as much as 40 mm of uplift on the east side of the south end of Coyote creek (Schmidt and Bürgmann, 2002). The InSAR data also show that uplift in the Santa Clara Valley is a seasonal phenomenon (Schmidt and Bürgmann, 2002).

Past earthquake-induced liquefaction and ground failure in the study area

Ground failure associated with the 1868 Hayward, 1906 San Francisco, and 1989 Loma Prieta earthquakes includes sand boils, disturbed wells, settlement, lateral spread, stream bank failure and ground cracks. The majority of ground failure phenomena observed in the study area caused by the 1868, 1906 and 1989 earthquakes is concentrated in the northern half of the study area near the margin of the San Francisco Bay, where ground water levels are typically within 3-4 meters of the ground surface (Figure 5).



**PEER STUDY AREA - Northern Santa Clara Valley,
San Francisco Bay Region, California**
**Historic Ground Failure in the Bay Area
(Knudsen and Others, 2000, Appendix C)**

◀▶ Lateral Spread
 ★ Settlement
 No deformation

Figure 5. Historic ground failure in the northern Santa Clara Valley (modified from Knudsen et al., 2000).

Ground failure associated with the 1868 Hayward earthquake includes lateral spreading and sand boils. Lateral spreading was observed along the banks of Coyote Creek, south of State Highway 237 in the vicinity of Barber Lane and north of State Highway 237 in the vicinity of Alviso-Milpitas Road (Knudsen and others, 2000). Reports of lateral spread describe the banks of Coyote Creek being shaken together and cracks with water pouring out following the bay side of the creek (Youd and Hoose, 1978). Sand boils were observed north of State Highway 237 in the vicinity of Alviso-Milpitas Road and near the intersection of Old Oakland Road and Atterberry Lane (Knudsen and others, 2000). Sand boils that occurred along cracks near Alviso-Milpitas Road flowed with water for 48 hours following the earthquake, while those that occurred along Old Oakland Road spurted water ‘...to the height of several feet’ (Youd and Hoose, 1978).

Ground failure associated with the 1906 San Francisco earthquake (reported in the compilation by Youd and Hoose, 1978) was more varied and more wide spread than that associated with the 1868 Hayward earthquake, and included stream-bank landsliding, lateral spread, ground settlement, ground cracks, sand boils and disturbed wells. Lateral spreads were observed north of State Highway 237 east of Ranch Road, as well as approximately 150 meters north of the bridge where Alviso-Milpitas Road crosses State Highway 237 (Knudsen and others, 2000). Approximately 400 meters north of the bridge

the entire road failed eastward into Coyote Creek (Youd and Hoose, 1978). South of State Highway 237 along Alviso-Milpitas Road between Zanker Road and Barber Lane (Knudsen and others, 2000) fissures opened up across an orchard, and some of the trees were out of alignment (Youd and Hoose, 1978). Also, approximately 500 m west of where present-day State Highway 237 crosses over Coyote Creek (Knudsen and others, 2000) cracks were observed (Youd and Hoose, 1978). Finally, south of Brocaw Road and west of Interstate 880 (Knudsen and others, 2000) a well was severed as the land shifted to the northwest (Youd and Hoose, 1978).

Estimates of ground settlement as a result of the 1906 San Francisco earthquake are documented at several locations within the study area. Settlement was observed along the train tracks leading out of the north end of the town of Alviso (Knudsen and others, 2000). Along First Street, towards the south east end of Alviso (Knudsen and others, 2000), a well casing was driven out of the ground (Youd and Hoose, 1978). Also in Alviso, in the vicinity of Moffat Street (Knudsen and others, 2000), settlement occurred in front of the principal hotel in town and along 1st Street between Innovation Dr. and Montague Expressway (Youd and Hoose, 1978). Approximately 500 meters west of where present-day State Highway 237 crosses over Coyote Creek (Knudsen and others, 2000) ground settlement was measured, and at the same location, the west side of a 3.7 meter diameter pool was lifted higher than the east side of the pool (Youd and Hoose, 1978). Settlement observed north of State Highway 237 along Alviso-Milpitas Road between Zanker Road and Barber Lane (Knudsen and others, 2000) caused a bridge piling to be uplifted (Youd and Hoose, 1978). South of State Highway 237 along Alviso-Milpitas Road between Zanker Road and Barber Lane (Knudsen and others, 2000) the northwest side of a ranch house settled slightly (Youd and Hoose, 1978). And finally, along Alviso-Milpitas Road between Zanker Road and Barber Lane (Knudsen and others, 2000) settlement was observed in fields (Youd and Hoose, 1978).

The 1906 San Francisco earthquake caused sand boils to occur at numerous locations. Near Alviso slough, in the vicinity of Alviso marina and Mill Road (Knudsen and others, 2000), cracks formed from which muddy and sandy water flowed (Youd and Hoose, 1978). Several sources describe cracks from which sandy water flowed (Youd and Hoose, 1978) in the vicinity of Coyote Creek, approximately 500 m west of where present-day State Highway 237 crosses over Coyote Creek (Knudsen and others, 2000). South of State Highway 237 along Alviso-Milpitas Road between Zanker Road and Barber Lane (Knudsen and others, 2000), cracks that developed in an orchard also flowed with sandy water (Youd and Hoose, 1978).

Miscellaneous effects of ground failure associated with the 1906 San Francisco earthquake consist of reports of disturbed wells. The pipe in an artesian well on the Fox farm located South of Brocaw Road, west of Interstate 880 (Knudsen and others, 2000), was severed 18.3 m below ground surface (Youd and Hoose, 1978).

Ground failure associated with the Loma Prieta earthquake of 1989 was somewhat limited in scope compared to the earthquakes of 1868 and 1906, however lateral spread and settlement were observed. South of San Jose Municipal Airport, minor lateral

spreading and settlement caused minor cracking along a frontage road (Seed and others, 1990). In addition, approximately 1 km north of San Jose Municipal Airport minor settlement of a tower foundation was observed (Seed and others, 1990). Finally, settlement was also observed in Alviso where settlement was observed in the approach fills of the Gold Street Bridge (Tinsley et al., 1998).

METHODS

A variety of methods are available to predict magnitudes of surface deformation resulting from liquefaction. All of these approaches begin with a geological and geotechnical characterization of the sediment in the study region (Figure 6).

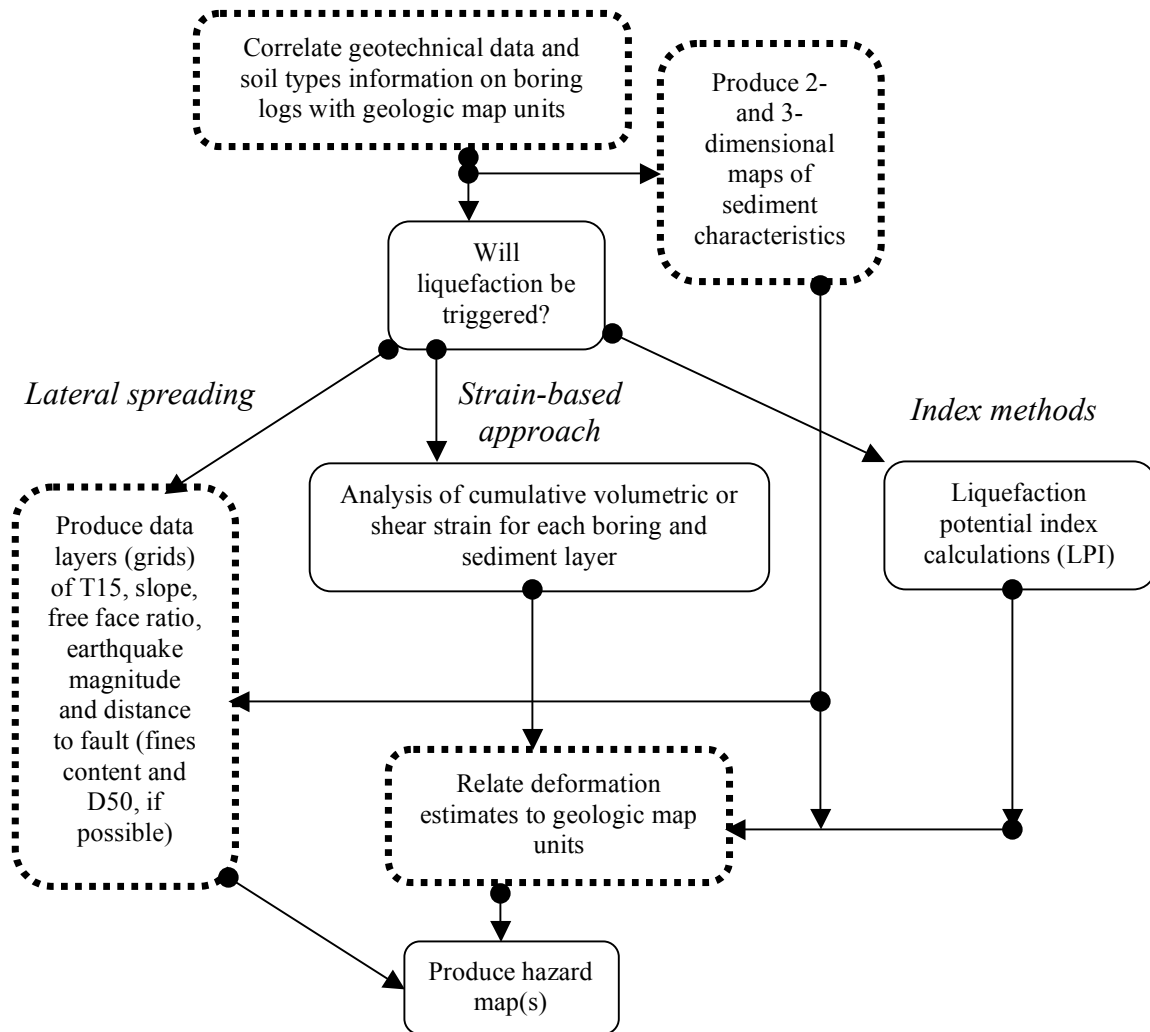


Figure 6. Methods employed during this feasibility study. Boxes that are dashed indicate points in the process where characterizing geologic and measurement variability is important.

Geologic and Geotechnical Characterization

To assess the potential for ground failure a thorough understanding of an area's Late Quaternary history and deposits is developed by interpreting logs of geotechnical borings and relating the stratigraphy depicted in the borings to surficial geologic map units. The information collected and used to interpret the geologic setting in this pilot study

includes: (a) detailed Quaternary geological mapping for the northern Santa Clara Valley area produced at 1:24,000 scale by Knudsen et al. (2000) and J.M. Sowers of William Lettis & Associates (unpublished), (b) more than 650 geotechnical borings, (c) probabilistic earthquake shaking information, (d) four types of digital terrain data, and (e) ground-water levels. Data used in this study are from the Milpitas, Calaveras Reservoir, San Jose East and San Jose West 7.5-minute quadrangles (Figure 1). Much of the boring data were collected from local government files and entered into a Geographic Information System during previous seismic hazard mapping efforts conducted by the California Geological Survey (<http://gmw.consrv.ca.gov/shmp/index.htm>).

The depth of the borings collected for this study ranged from 10 to 150 feet, with 40% reaching a minimum depth of 40 feet or more. Penetration test usefulness varies considerably from one boring and operator to the next. Recorded blow counts for non-SPT sampling, where the sampler diameter, hammer weight and drop distance and energy delivery differ from those specified for an SPT are converted to SPT-equivalent blow count values, when appropriate. To characterize the quality and usefulness of each SPT value, each penetration test compiled in the database is ranked from 1 to 29 based upon how closely the sampling matches ASTM D1586-99 standards, and whether or not the recorded blow counts can reasonably approximate those of an SPT. Any penetration test with a quality ranking lower than 12 is not analyzed. When no laboratory fines content analysis is provided for layers with liquefiable textures, a default fines content is assigned based upon the Unified Soil Classification Code (USCS) designation for the layer (Table 2). Similarly, if unit weight data is not provided along with boring logs then values for each layer, based on the layers soil type must be assumed (Appendix 1). The actual and converted SPT blow counts are normalized to a common reference effective overburden pressure of 1 atmosphere (approximately 1 ton per square foot), and a hammer efficiency of 60% using a method described in Seed and Idriss (1984) and updated according to the recommendations by Youd et al. (2001) and Seed et al (2003). This normalized blow count is referred to as $(N_1)_{60}$. Some of the methods for evaluating the susceptibility of deposits to liquefaction and the potential for deformation include correcting the $(N_1)_{60}$ value for the fines content of the sample; this value is referred to as $(N_1)_{60,cs}$. In a study like this in which only existing geotechnical borings are used, the quality of the borehole data varies. The logs should provide thorough documentation of how and where each boring was advanced. Also, laboratory studies of texture, grain size distribution and fines content (FC) provide information needed in several of the methods used to estimate liquefaction-induced deformation.

TABLE 2. FINES CONTENT (FC) ASSIGNED TO SAMPLES FOR WHICH NO TEXTURAL DATA WAS PROVIDED ON BORING LOGS

	Curve ^(a) used in triggering evaluation	FC ^(b) used in $(N_1)_{60,cs}$ calculation
Standard/conforming USCS categories		
GW, GP, SW, SP	SD	2.5
GW-GM, GW-GC, GP-GC, SW-SM, SW-SC, SP-SM, SP-SC	SM	8.5
GM, SM	SM	24
GC-GM, SC-SM	ML	30
GC, SC, ML	ML	35

Other non-standard USCS categories found on boring logs (c)		
GP-SP, GW-GP, SW-SP “cobbles & boulders”, “gravel”, “gravel and sand”, “sand”	SD	2.5
“artificial fill”, “soil”	SM	12
GP-SM, SM-SP	SM	14
SC-SP, SC-GP	SM	19
GM-SM, “alluvium”, “loess”	SM	24
ML-SM, SM-SC	ML	30
ML-CL, SC-CL, SC-ML, SM-CL, SM-ML	ML	35

(a) curve assigned for use in Simplified Procedure triggering analysis (SD- 5%, SM - 15%, ML - 35% fines content)

(b) fines content assigned (when no laboratory textural data is available) for use in calculating $(N_1)_{60,cs}$

(c) soil descriptions found on boring logs that do not conform with USCS categories; these categories are not recommended for use in logging borings

To characterize sediment in the area, each layer in the compiled database of geotechnical boring logs is assigned a geologic map unit (Figure 7). This geologic characterization of materials depicted on the boring logs is based on interpretation of several characteristics, including: texture, penetration resistance, color, indications of soil development, presence of regionally identifiable units (e.g. Bay Mud) and regionally correlatable changes. After each layer is assigned a geologic map unit designation, the shallowest depth of the youngest Pleistocene unit (if present) in each boring is identified. The Pleistocene surface is regarded as the depth where there is a discernable change in the geotechnical properties of the sediment, the most telling change being an increase in the density of deposits or the presence of a paleosol. It was possible to tentatively identify the contact between Holocene and Pleistocene sediment in 215 of 668 borings used in this study. Using these data maps of the thickness of Holocene sediment or the elevation of the top of the Pleistocene are developed (e.g. Figure 8). The Pleistocene surface elevation is an important horizon to identify in California because most researchers believe that sediment greater than 11,000 years old is unlikely to liquefy. Pleistocene sediment typically is denser, more cemented, and has been shaken many times by large earthquakes. Because of a limited number of borings that penetrate to significant depths where the Pleistocene surface is deepest in the center of the valley (Figure 8), these contours are constructed with much less confidence than those near the valley edges.

In order to relate properties from boring logs to geologic map units boring logs and the sediment within them are classified three ways (Figure 7). Every layer on boring logs is assigned a geologic map unit. Each boring is assigned a geologic map unit based on which map unit is mapped at the surface where the boring was advanced. This map unit is derived by intersecting two GIS layers: the Quaternary geologic map, and the locations of the boring logs. Finally, each boring log is assigned a “representative age” based on whether the bulk of the sediment in the boring is interpreted to be Holocene, Pleistocene or artificial fill.

Boring Surface unit - artificial fill (af)
 Boring Assigned Representative age – Holocene (Qh)

Assigned geologic map
 unit to each layer

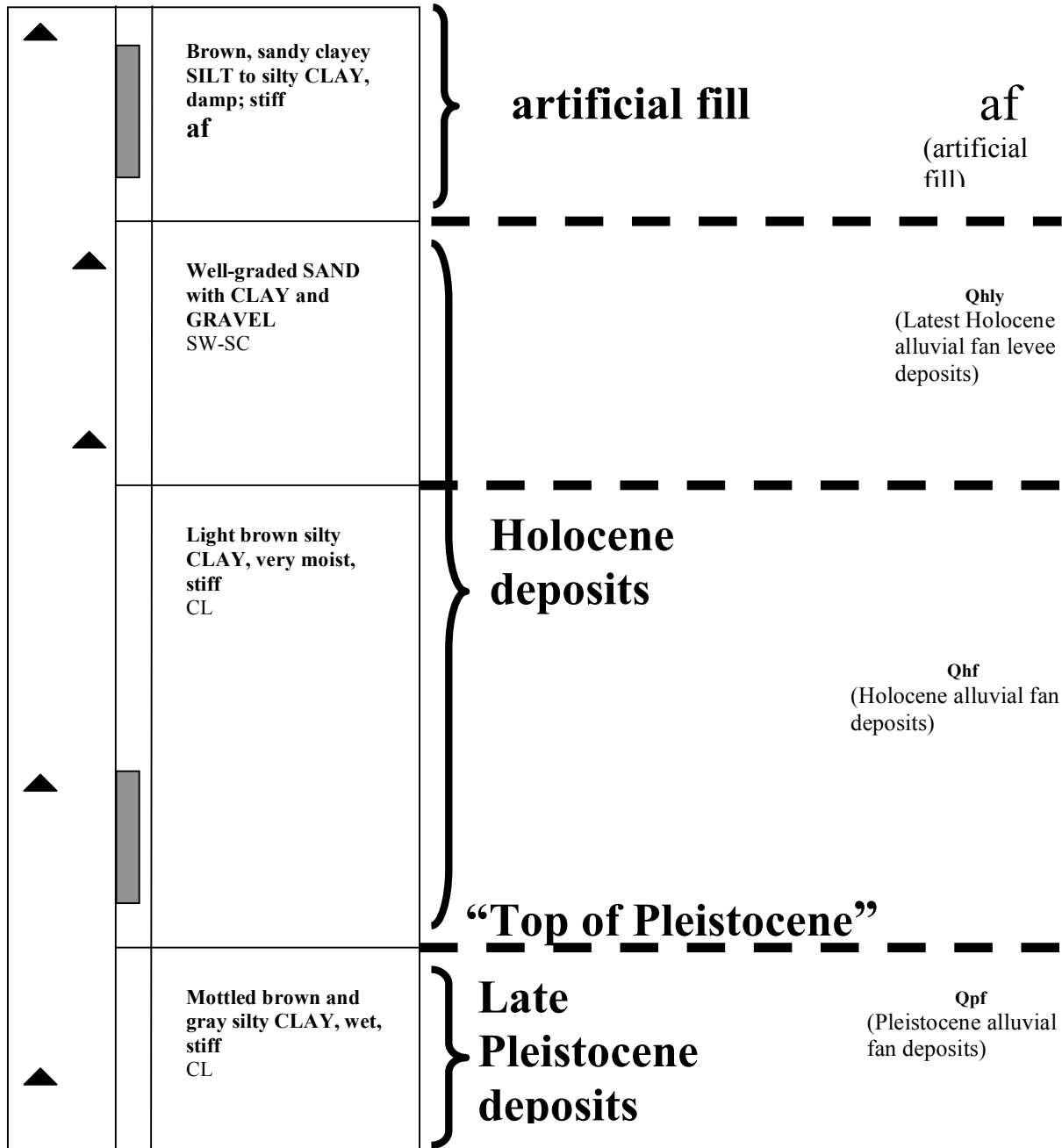


Figure 7. Geotechnical boring log and relating layers and borings to geologic map units.

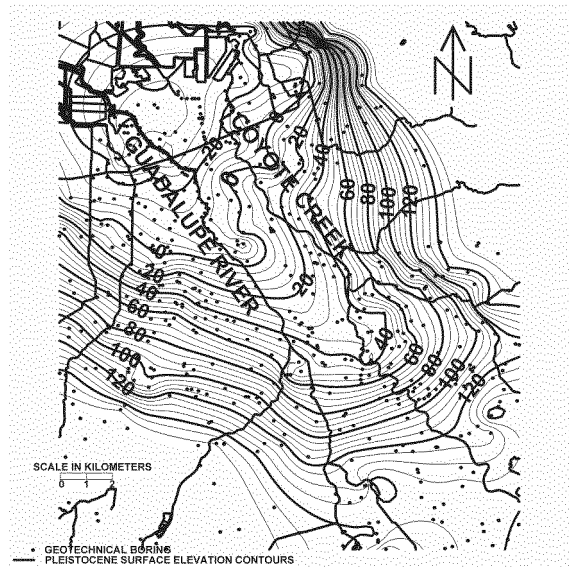


Figure 8. Pleistocene surface elevation in feet (modified from Clahan et al., 2002)

Liquefaction assessments

As shown in Figure 9, there are two classes of methods for estimating quantities of post-liquefaction ground deformation, both of which are typically used in site investigations, not in regional mapping; these are (1) predictions of volumetric and shear strains, and (2) empirical predictions of lateral spread displacements. Predictions of strain can be made using either semi-empirical formulations or numerical simulations. All of these methods rely on calculations using parameters and data that are collected by consultants doing site specific investigations and geotechnical borings. To assess liquefaction hazard, a range of geotechnical parameters is calculated for the layers within each boring and for the boring as a whole. The liquefaction potential of each layer in every boring is evaluated deterministically using the methods of Youd et al. (2001) and probabilistically using the methods of Seed et al. (2003). Parameters calculated for each boring include the thickness of sediment with liquefiable textures, the thickness of saturated liquefiable sediment (does not include layers identified as CH, CL, MH), the predicted liquefaction-induced volumetric strain, the limiting shear strain and the liquefaction potential index (LPI).

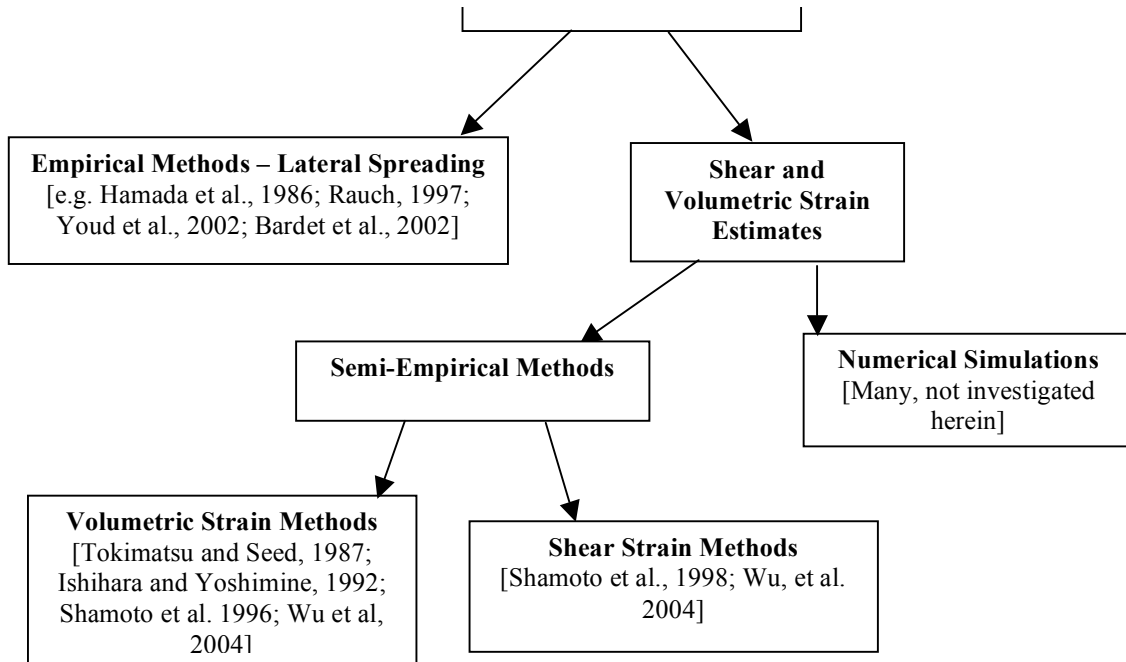


Figure 9. Methods of predicting liquefaction-induced deformation

Predictions of volumetric and shear strain

Semi-empirical methods for predicting shear and volumetric strain are based on a growing set of laboratory data, improved understanding of processes. Some of these methods have been calibrated against the growing database of ground failure case histories. Probabilistic liquefaction triggering analysis and analysis of settlement for non-saturated soils also may be incorporated into these methods. The major disadvantages of applying the semi-empirical methods to estimate shear and volumetric strain are that these methods require detailed geotechnical data (for best results laboratory data is used) that can be expensive to collect. Semi-empirical means for predicting shear and volumetric strain include those of Tokimatsu and Seed (1987), Ishihara and Yoshimine (1992), Shamoto et al. (1996, 1998), Wu (2002), Wu and Seed (2004), and Wu et al. (2004).

The approach proposed by Tokimatsu and Seed (1987) for estimating post-liquefaction ground deformation uses correlations developed from field case studies and laboratory test data. Their case studies are for settlement only, and are associated with the 1964 Niigata and 1968 Tokachi-oki and Miyagiken earthquakes. This approach provides easy to read charts for both shear and volumetric strain and can be used for saturated and unsaturated conditions. Among the drawbacks of this method are that it predicts “limiting strain”. As Wu (2002) explains, limiting strain depicted on the chart by Tokimatsu and Seed (1987) is not the “ultimate” strain, but the “...maximum single amplitude cyclic shear strain within 15 loading cycles”. The curves are calibrated for clean sands, and no fines content correction is provided. It is possible to convert measurements for impure sand to the clean sand equivalent, but this process introduces greater uncertainty in the final result.

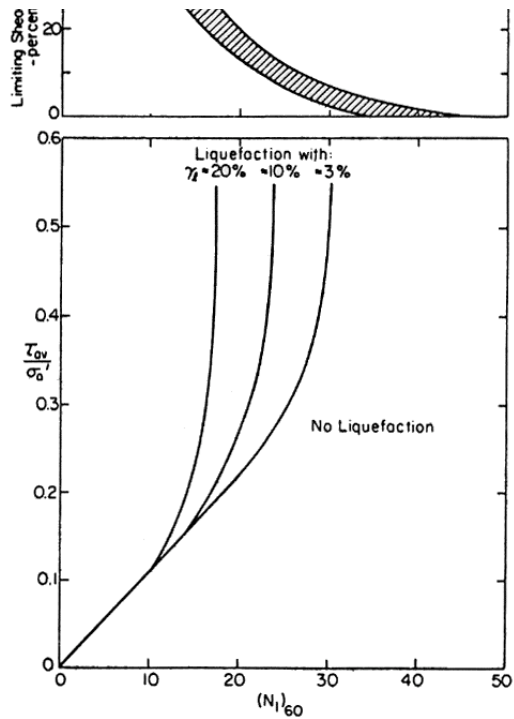


Figure 10. Tokimatsu and Seed (1984) method of predicting volumetric strain and limiting shear strain (from Tokimatsu and Seed, 1984)

The approach proposed by Ishihara and Yoshimine (1992) is based on results of laboratory simple shear data that was calibrated against observed settlement caused by the 1964 Niigata earthquake. Shear and volumetric strain can be read off the family of curves formulated by Ishihara and Yoshimine (1992) if the factor of safety against liquefaction and density of the soil are known. The chart shows a maximum shear strain of 3.5% where the factor of safety against liquefaction is 1. The major disadvantages of this method are that it yields a prediction of maximum strain rather than residual strain, and like Tokimatsu and Seed (1987) offers no fines content correction.

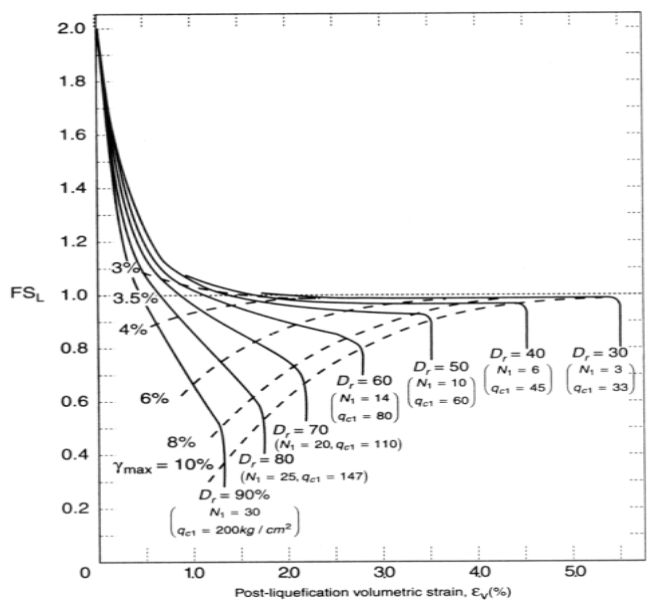


Figure 11. Ishihara and Yoshimine (1992) method for predicting volumetric and shear strain (from Ishihara and Yoshimine, 1992)

The Shamoto et al. (1998) method evolved from the work of Tokimatsu and Seed (1984) and it relies on new constitutive analyses with laboratory data and case studies from the 1995 Hyogoken-Nambu earthquake. The basis for this method is the interdependency of maximum shear strain and post-liquefaction shear and volumetric strain. The magnitude of post-liquefaction strain, both shear and volumetric, is primarily dependent upon irreversible dilatancy, suggesting that the resulting post-liquefaction residual ground settlement and horizontal displacement should not be studied separately. The advantages of this method are that it provides easy to read charts (Figures 12 and 13) for both clean and ‘dirty’ sands, and equations for both level ground and liquefiable sandy ground near a waterfront or free face.

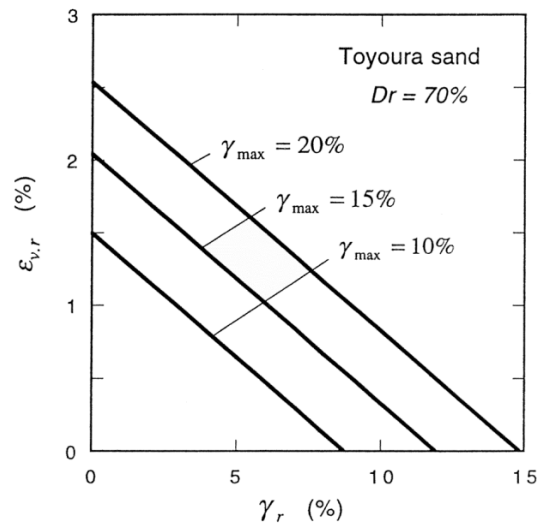


Figure 12. Shamoto et al. (1998) chart showing the interdependency of volumetric and shear strains for different levels of irreversible dilatancy (from Shamoto et al., 1998)

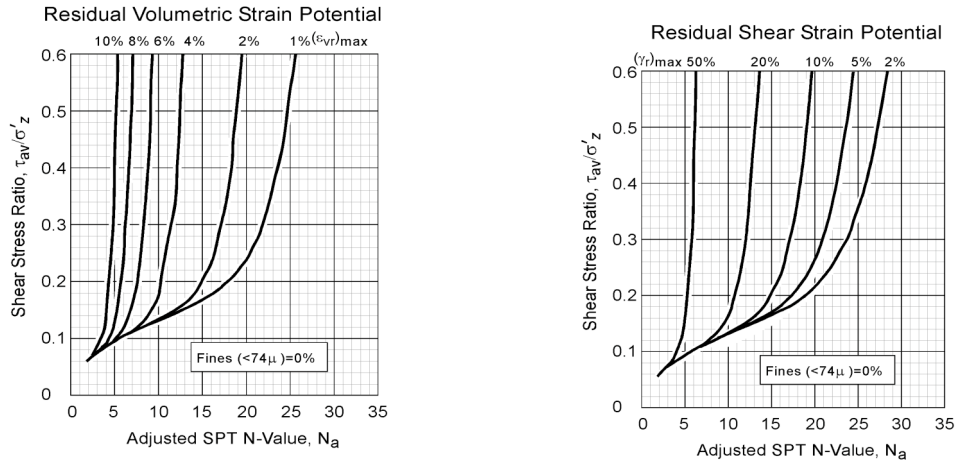


Figure 13. Shamoto et al. (1998) relationships used to predict residual volumetric and shear strain (from Shamoto et al., 1998)

The Wu (2002), Wu and Seed (2004), and Wu et al. (2004) methods are based on laboratory testing of undrained, cyclic simple shear testing on fully saturated sand. Wu (2002) conducted tests using Monterey No. 0/30 sand, with strain measured at 15 cycles, (approximating an M 7.5 earthquake), pressures of 40kPa, 80kPa and 180kPa, and relative densities ranging from 35% to 80%. The results of the testing show that calculated strain (for level ground conditions) falls within the ranges predicted by the limiting strain charts formulated by Tokimatsu and Seed (1987). Among the benefits of this method are that in addition to providing an estimate of probability of liquefaction (P_L), it includes updates to previously developed tools including a new nonlinear shear mass participation factor (R_d) and new fines correction factor (C_{fines}).

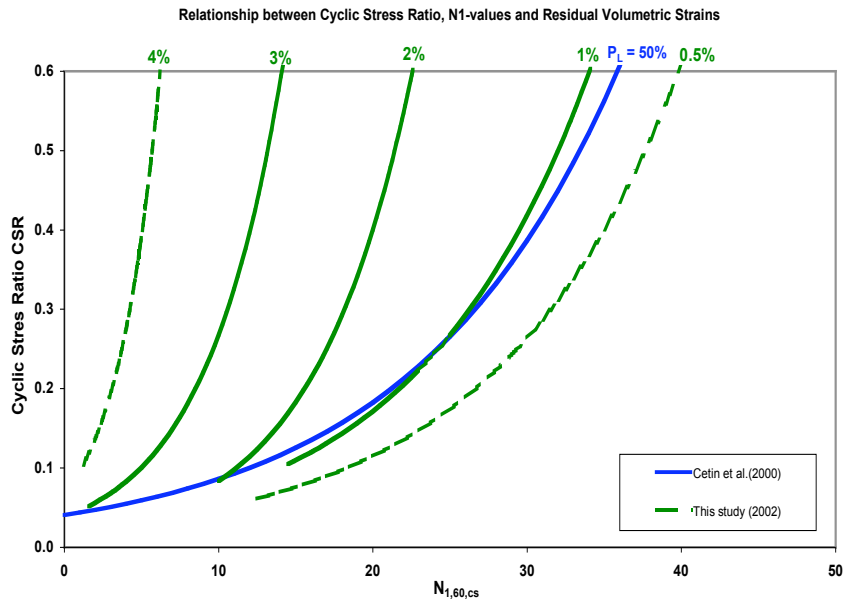


Fig. 14. Proposed correlations between CSR, $(N_1)_{60,cs}$ and reconsolidation volumetric strain (from Wu et al., 2004).

The Wu et al. (2004) method to estimate volumetric strain involves four steps: (1) evaluate liquefaction susceptibility for each saturated layer, (2) the values estimated in step one are used in conjunction with a new family of curves (Figure 14) to estimate the post-liquefaction reconsolidation volumetric strain of each saturated, liquefiable layer; (3) volumetric compression of non-saturated sandy layers can be calculated according to the Tokimatsu and Seed (1987) procedures, and (4) the volumetric changes of all saturated and unsaturated soil layers is summed. The new procedure was shown by Wu and Seed (2004) to perform well for a suite of field performance case histories with small-to-moderate ground settlements.

Wu (2002) also proposed a new pragmatic chart for prediction of limiting shear strain (Figure 15). This chart, however, is preliminary because it has yet to be thoroughly calibrated against field performance case histories, and as a result, may be updated or modified in the future. The Wu (2002) procedure to calculate limiting shear strain parallels the procedure described above to calculate volumetric strain.

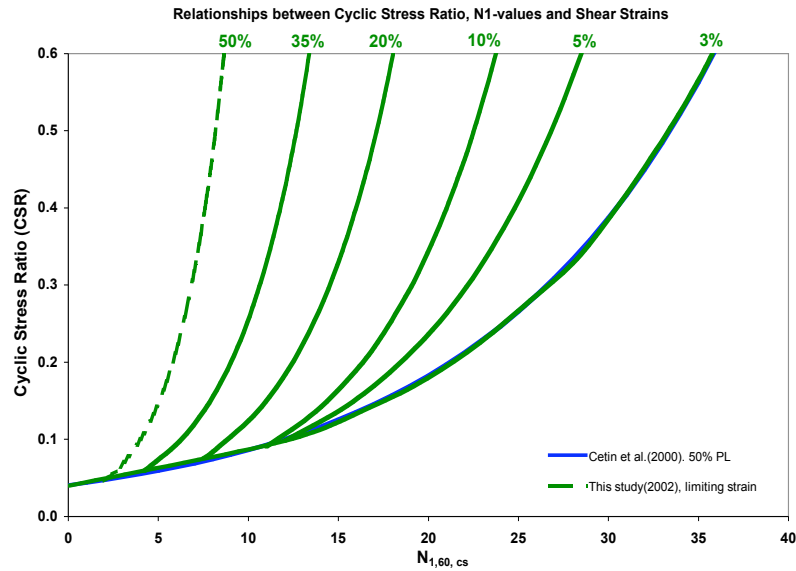


Fig. 15. Proposed correlations between CSR, $(N_1)_{60,cs}$ and limiting strain (from Wu, 2002).

In this project, all six methods listed in Table 3 (two for shear and four for volumetric strain) were used and results compared. However, in this paper, the values estimated using the Wu et al., (2004) and Wu (2002) approaches for volumetric and shear strain are presented and used to characterize Quaternary geologic map units and produce example maps of deformation. It should be noted that, the methods for estimating volumetric strain yield results that can be thought of as “predicted” or as “within-a-factor-of-two,” whereas the relationships used to estimate future shear strain should be thought of as “limiting” or “potential” values.

TABLE 3. CALCULATION OF STRAIN PARAMETERS AND THE METHODS USED TO CALCULATE THEM IN THIS PROJECT

Parameter	Volumetric Strain (Settlement) Methods				Shear Strain (Horizontal Displacement) Methods	
	Wu et al., 2003	Ishihara & Yoshimine, 1992	Shamoto et al., 1998	Tokimatsu & Seed, 1987	Wu et al., 2004	Shamoto et al., 1998
N	$N_{1,60,cs}$ (Seed et al., 2003)	$N_{1,60,cs}$ (Seed et al., 2003)	$N_{1,60}$ translated to Na	$N_{1,60,cs}$ (Seed et al., 2003)	$N_{1,60,cs}$ (Seed et al., 2003)	$N_{1,60}$ translated to Na
FC	Seed et al., 2003	Seed et al., 2003	Shamoto et al., 1998	Youd et al. 2001	Seed et al., 2003	family of curves
CSR	probabilistic Seed et al., 2003	probabilistic Seed et al., 2003	Youd et al. 2001	Youd et al. 2001	probabilistic Seed et al., 2003	Youd et al., 2001
R_d	Seed et al., 2003	Seed et al., 2003	Youd et al. 2001	Youd et al. 2001	Seed et al., 2003	Youd et al., 2001
Output type	predicted	predicted	predicted	predicted	potential/ limiting	potential/ limiting

Lateral spread predictions

Empirical models for predicting lateral spread displacements require topographic (e.g. ground slope, free face ratio), seismological (e.g. earthquake magnitude, distance to rupture, peak horizontal ground acceleration), and geotechnical boring (e.g. thickness of liquefiable layers with $(N_1)_{60} < 15$, mean grain size of sediment for layers with $(N_1)_{60} < 15$, fines content [FC] for layers with $(N_1)_{60} < 15$) input. Among the advantages of empirical approaches are that the models are based upon extensive field case history studies and the models improve as the database expands. These methods are relatively easy to implement at the site-specific level. The drawbacks of such an approach are a tendency to over-simplify geotechnical data and analysis and the lack of support for formal probabilistic analysis. Examples of empirical means for predicting lateral spread include Hamada et al. (1986), Bartlett and Youd (1992), Rauch (1997), Bardet et al. (1999, 2002), and Youd et al. (1999, 2002).

The method selected to estimate lateral ground displacement for this pilot study is a four-parameter empirical model developed by Bardet et al. (1999). The model is used to predict liquefaction-induced ground displacement under both free face and sloping ground conditions. The four-parameter model is derived from a multiple linear regression analysis of data sets consisting of measured ground displacement, topographical data, borehole data and seismological data. The four-parameter model was used in this study because the six parameter models include estimates of mean grain size (D_{50}) and fines content (FC) of sediment for layers with $(N_1)_{60} < 15$. This data is rarely available from boring logs submitted with development-related consulting reports on file in the offices of local building departments. The equation for the Bardet et al (1999) four-parameter model is:

$$\text{Log}(D + 0.01) = b_0 + b_{\text{off}} + b_1 M + b_2 \log(R) + b_3 R + b_4 \text{Log}(W) + b_5 \text{Log}(S) + b_6 \text{Log}(T_{15})$$

where D is the horizontal displacement (in meters); M the moment magnitude; R the nearest horizontal distance to a seismic source (in kilometers); S the slope of the ground surface (in %); W the free face ratio (in %); and T_{15} is the thickness (in meters) of saturated cohesionless soils with $(N_1)_{60} < 15$. The term $\text{Log}(S)$ is set equal to zero for free face cases and the term $\text{Log}(W)$ is set equal to zero for ground slope cases. The coefficient b_{off} is used only for free face conditions and is set equal to zero for ground slope cases. Figure 16 shows how the topographical parameters are calculated.

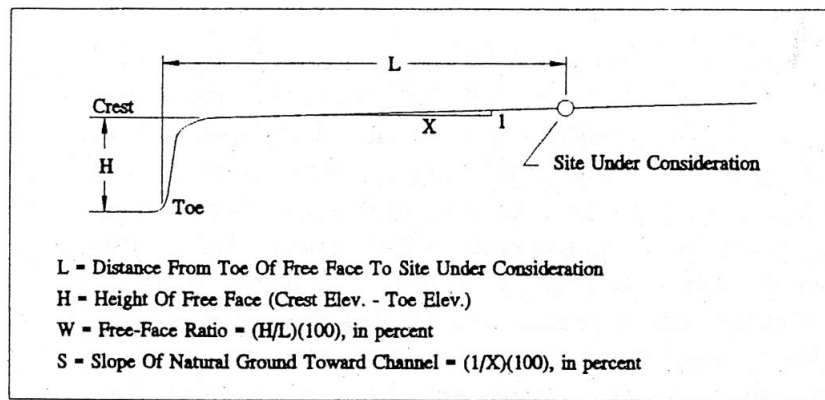


Figure 16. Defining ground slope (S) and free face ratio (W), from Bartlett and Youd, 1992)

The values of the coefficients proposed by (Bardet and others (1999) are:

b_0	-6.815	b_3	-0.026
b_{off}	-0.465	b_4	0.497
b_1	1.017	b_5	0.454
b_2	-0.278	b_6	0.558

Youd et al (2002) also proposed a 6-parameter model. This model also includes fines content (FC) and median grain size (D50) of the saturated soils with liquefiable textures.

A sensitivity analysis was performed to evaluate the relative importance of the parameters in both the Youd et al. (1999) six-parameter model and the Bardet et al. (1999) four-parameter model. A 1999 version of the Youd et al. model was used; there is a more current version presently available (Youd et al., 2002). In the sensitivity analysis, one parameter was varied through the range of allowable values while the other three or five parameters were kept constant at values thought to be representative of conditions in the Santa Clara Valley. Several general conclusions can be derived from Figure 17:

- (1) The Bardet et al. (1999) and Youd et al. (1999) models produce similar results,
- (2) The Youd et al. (1999) predicted values tend to be slightly lower than the Bardet et al. (1999) predicted values,
- (3) The models are most sensitive to the earthquake magnitude (M) and distance to causative fault(R) parameters, and
- (4) Predictions are more sensitive to changes in slope (S) when slope values are less than about 2.5 to 3% and to changes in free face ratio (W) when free face values are less than about 10%.

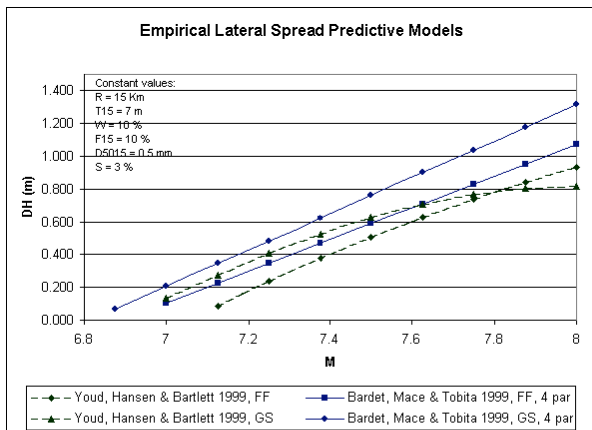
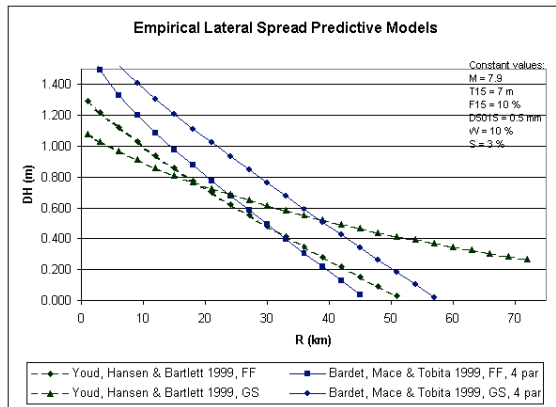
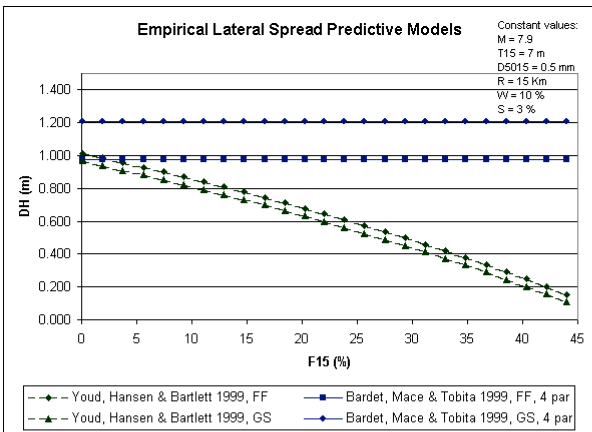
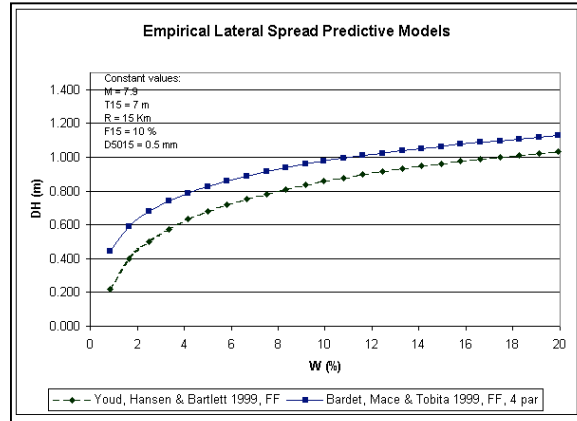
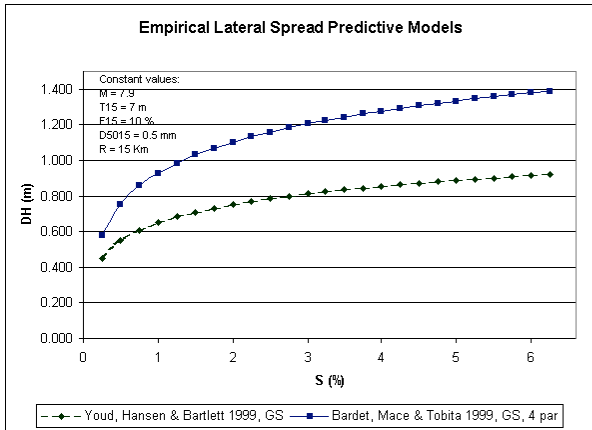
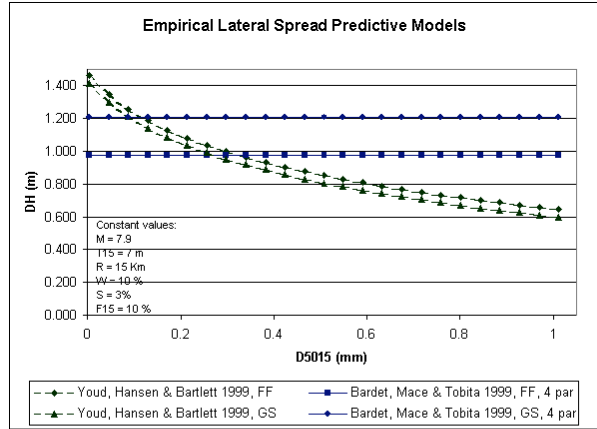
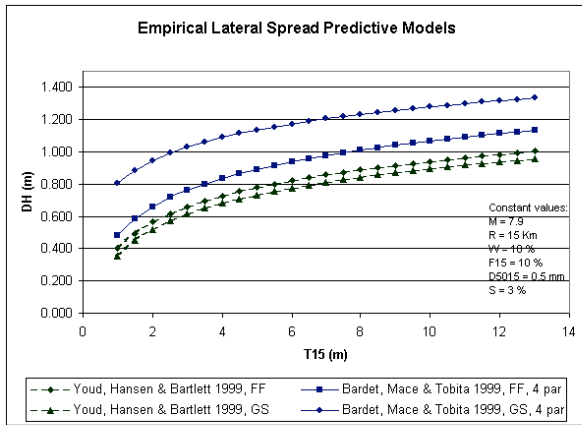


Figure 17. Parameter sensitivity analysis, four and six parameter lateral spread models, for sloping ground (GS) and free face (FF) conditions.

Liquefaction Potential Index approach

Liquefaction Potential index (LPI, but in Japan commonly referred to as P_L), originally defined by Iwasaki et al. (1982), provides an estimate of the severity of liquefaction at a specific location. The purpose is not to predict the occurrence of liquefaction, but rather to indicate the potential for damage as a result of liquefaction. The LPI calculation takes in to account the thickness of the liquefied layer(s), the proximity of the liquefied layer(s) to the ground surface and the factor of safety for the layer(s). The calculation requires that a boring being assessed should be 20 m in length. Severe liquefaction and ground deformation is likely at sites where LPI exceeds 15.

Toprak and Holzer (2003) combine the method defined by Iwasaki et al. (1982) with CPT data collected from sites where liquefaction occurred during historic earthquakes in California. Toprak and Holzer (2001) found that a site with an LPI value of 15 has a 93% probability of exhibiting surface manifestations of liquefaction, while a site an LPI value of 5 has only a 58% probability of exhibiting surface manifestations of liquefaction.

RESULTS

Properties of study area sediment – Descriptive statistics

In the northern Santa Clara Valley there are 26 Quaternary map units that are mapped by Knudsen et al. (2003) and J.M. Sowers (unpublished). In the northwestern part of the study area, the most areally extensive deposit is Holocene San Francisco Bay Mud (Qhbm). In the central, southeastern and southwestern portions of the study area Holocene alluvial fan deposits (Qhf), and Holocene alluvial fan deposits, fine facies (Qhff) are the most widely mapped units. Young, historically inundated deposits (Qhty, Qhly, Qhfy) are mapped along the two major streams (Guadalupe River and Coyote Creek).

Table 4 shows that for many of the geologic map units less than half of the sediment layers described on the compiled boring logs are coarse enough to liquefy (i.e. not USCS classes CL, CH, MH, ML-CL, OH, OL, Pt). This is true whether one analyzes the sediment texture by looking at numbers of layers or total boring length assigned to each map unit. Map units that are expected to be fine grained (e.g. Qhb – Holocene basin deposits, Qhff – Holocene alluvial fan, fine facies, Qhbm – Holocene Bay mud) all consist of greater than 80 to 85% fine sediment.

Table 4 Percentage of each geologic map unit with textures that are potentially liquefiable

Geologic map unit	Number of layers		Layer thickness	
	# of layers	% of layers with liquefiable texture (%)	Cumulative thickness of all layers (m)	% of total with liquefiable textures
af	223	26	329	14
alf	11	55	21	57
Qhc	20	65	53	55
Qhfy	46	22	78	13
Qhly	169	37	323	28
Qhty	87	44	129	31
Qhbm	29	7	51	9
Qhb	17	18	35	7
Qhfe	103	31	160	18
Qhf	1700	47	2925	42
Qhff	267	14	488	10
Qhl	357	53	611	48
Qht	8	88	8	92
Qf	116	46	415	37
Ql	12	50	17	39
Qt	2	100	2	100
Qpf	561	59	1304	58

See Table 1 for geologic map unit definitions, units are listed in order of increasing age

Table 5 shows penetration resistance measurements that have been transformed to $(N_1)_{60,cs}$ values using the Seed et al. (2001) and Youd et al. (2001) methods. This table also shows the calculated average factor of safety for all layers with liquefiable textures (zero values for layers with textures too fine to liquefy were not averaged).

TABLE 5. FINES CORRECTED PENETRATION RESISTANCE, FACTOR OF SAFETY AND CYCLIC RESISTANCE RATIO FOR ALL GEOLOGIC MAP UNITS											
	Penetration Resistance ($(N_1)_{60,cs}$)						Factor of Safety (only liquefiable textures)		Cyclic Resistance Ratio (CRR)		
	All textures (including fines)			Only liquefiable textures							
Geologic map unit	# of layers median [Seed et al., 2003]		median [Youd et al., 2001]		% of layers median [Seed et al., 2003]		# of FS values mean FS median FS		mean median standard deviation		
af	24	10.4	13.1	63	11.9	42	0.7	0.3	0.27	0.15	0.29
alf	4	6.3	9.8	75	8.5	5	0.2	0.2	0.12	0.09	0.05
Qhc	4	11.2	11.6	100	11.2	11	0.5	0.4	0.36	0.23	0.36
Qhfy	4	11.1	14.8	100	11.1	7	0.6	0.4	0.16	0.17	0.04
Qhly	20	6.5	9.5	95	6.5	51	0.4	0.3	0.21	0.17	0.19
Qhty	12	7.0	9.4	100	7.0	27	0.3	0.2	0.20	0.15	0.19
Qhbm	1	8.5	12.1	0	na	na	na	na	na	na	na
Qhb	2	6.2	9.7	50	7.9	4	0.2	0.2	0.15	0.15	na
Qhfe	5	4.8	7.9	100	4.8	15	0.2	0.2	0.18	0.12	0.24
Qhf	312	11.2	14.2	89	11.6	553	0.5	0.3	0.35	0.20	0.33
Qhff	11	8.7	12.3	55	9.5	31	0.4	0.3	0.24	0.18	0.24
Qhl	83	10.3	13.8	90	10.3	135	0.4	0.3	0.27	0.17	0.27
Qht	4	28.9	31.1	100	25.3	4	1.0	1.2	1.00	1.00	na
Qf	22	10.8	13.6	100	10.8	40	0.4	0.3	0.23	0.22	0.17
Ql	3	8.5	12.1	100	8.5	4	0.2	0.2	0.15	0.14	0.03
Qt	2	26.3	28.8	100	26.3	2	0.7	0.7	na	na	na
Qpf	129	19.2	21.5	93	19.8	222	0.9	0.7	0.56	0.35	0.39

See Table 1 for unit definitions, units are listed in order of increasing age; μ – mean; med – median; σ – standard deviation
 Textures that are not subject to liquefaction include CL, CH, MH, ML-CL, OH, OL, Pt

Several trends are evident in Table 5: (1) $(N_1)_{60,cs}$ values for sediment with liquefiable textures are generally low, in most cases the median values are less than 15 - a value previous researchers have considered an upper bound for sediment likely to experience large-scale liquefaction-related deformation. (2) The method of Youd et al. (2001) results in median $(N_1)_{60,cs}$ values that tend to be 2 to 3 blows/ft higher than the values calculated using the method of Seed et al. (2003). (3) The median FS value for most geologic map units is much less than 1, indicating that the layers in this area with potentially liquefiable textures are prone to liquefaction when shaken at the 10% exceedence in 50 years levels. However it is important to remember that a significant fraction of the sediment in the study area is composed of fine-grained materials – materials that are likely too fine to liquefy.

Figure 18 shows histograms of all penetration resistance (from layers with liquefiable textures) measurements collected for this project. Each layer has been assigned a geologic map unit based on interpretation of the stratigraphy depicted in the boring logs. The histograms for map unit for which there are a sufficient number of samples (e.g.

Qhly, Qhfe, Qhf, Qhl suggest that $(N_1)_{60,cs}$ populations are not normally distributed, but are more likely to be log-normally distributed. There appears to be general trend of increasing penetration resistance with increasing age of deposits, as observed in Table 5. These plots make it clear that discriminating one sample from another, based on the interpreted geologic map unit, is not an easy task. For this reason, a “box and whisker” plot of these same data was developed (Figure 19). This box and whisker plot shows that only a few of the map units can be readily distinguished from other map units based on the fines corrected penetration resistance parameter.

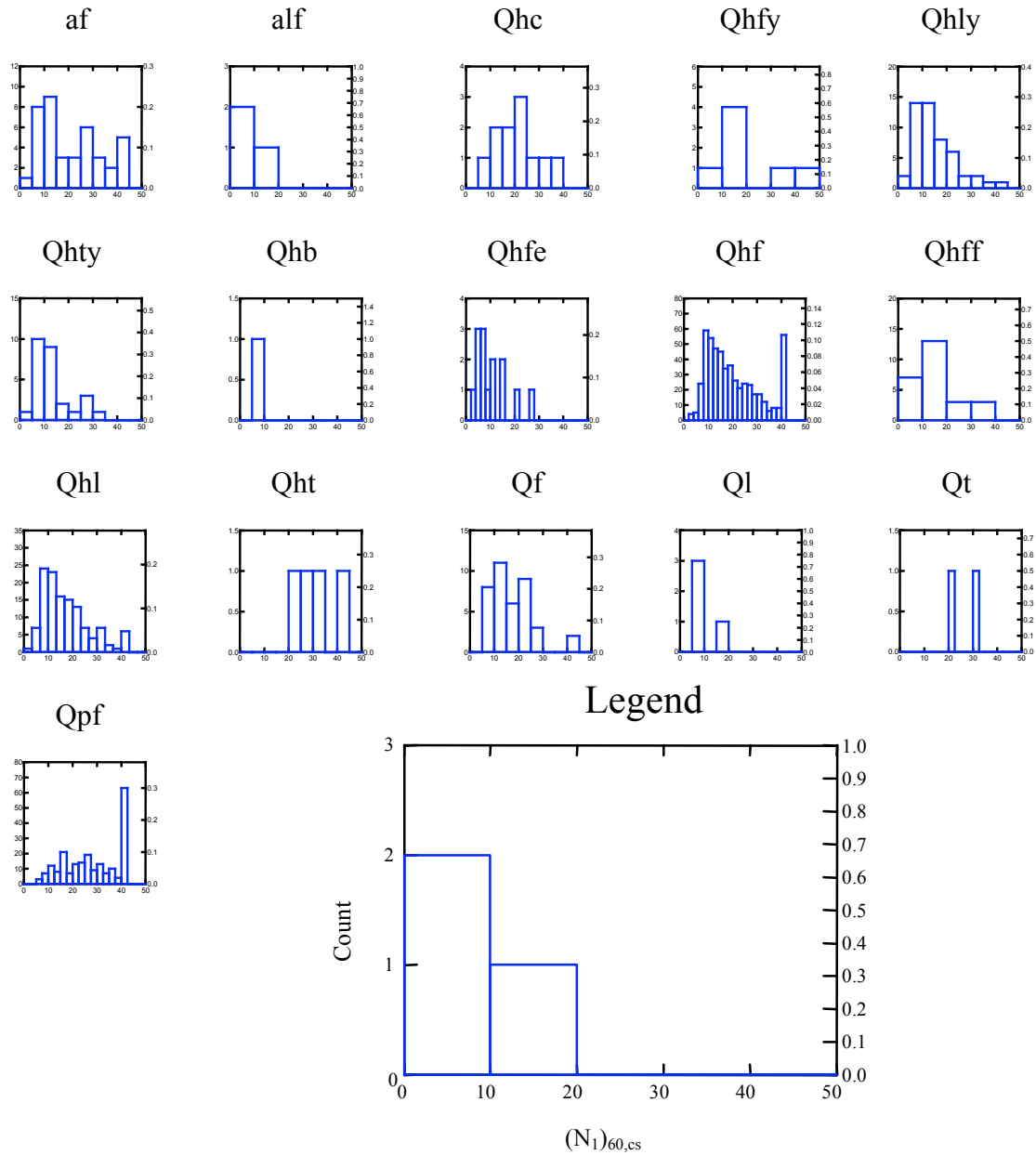


Figure 18. Histograms showing fines corrected penetration resistance $[(N_1)_{60,cs}]$ for every layer in the project database of geotechnical borings

Figure 20 presents another way to look at penetration resistance measurements. In Figure 20, all artificial fill layers are aggregated, all Holocene layers are aggregated and all Late Pleistocene layers are aggregated. These plots clearly show that the penetration resistance is not normally distributed; rather it appears to be log-normally distributed. A comparison of the Holocene and Pleistocene plots (middle and right most plots, respectively) shows that Pleistocene deposits tend to be slightly more resistant to penetration.

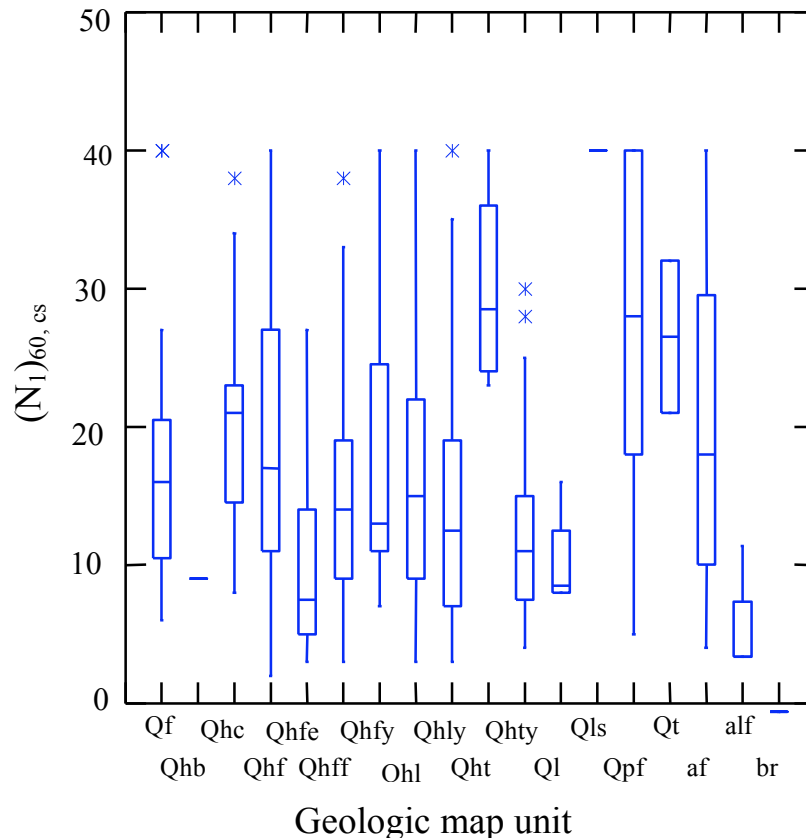


Figure 19. Box and whisker plot of fines corrected penetration resistance measurements for every layer in the project geotechnical boring database. The length of the box shows the first inter-quartile range; the line through the box shows the median value

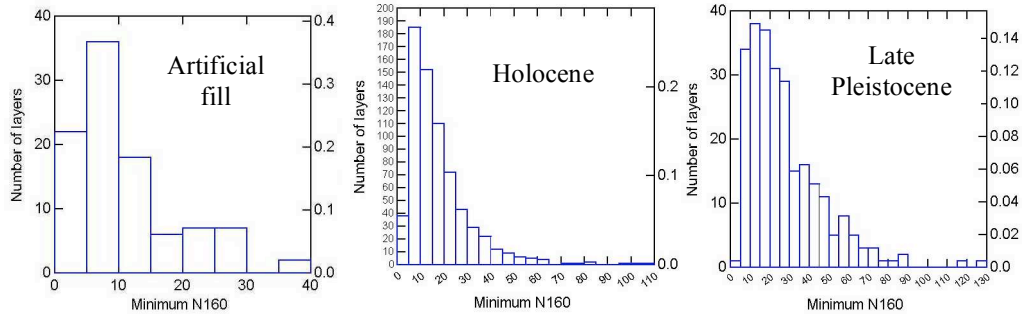


Figure 20. Histograms of penetration resistance (by layer, only liquefiable textures are included). From right to left artificial fill [n=98, mean=11.5, median=8.9], Holocene deposits [n=693, mean=17.7, median=14.1], and Latest Pleistocene deposits [n=255, mean=28, median=23].

Estimating strain for each geologic map unit

Table 6 summarizes some of the data generated by the liquefaction-induced ground deformation model (Wu 2002) used in this study. Table 6 relates strain calculations for borings to the mapped and interpreted geology in two ways: (a) all borings are grouped according to which geologic map unit is mapped at the surface where the boring was advanced, and (b) each boring is characterized by its “representative age”. A boring’s representative age is established after each layer described on the boring log is assigned a geologic map unit. Then the thickness of artificial fill, Holocene and Pleistocene deposits is calculated and whichever is greater is assigned as the boring’s representative age. The volumetric strain results were produced using the Wu et al. (2004) method; the limiting shear strain results were produced using the methods described in Wu (2002). To estimate amounts of settlement or horizontal displacement one simply multiplies the calculated strain by the thickness of saturated sediment with potentially liquefiable textures. Data from these tables are used to produce maps depicting volumetric strain (Fig 21) and settlement (Fig 22). The data presented in Table 6 can be used to produce maps of shear strain and/or horizontal displacement, however, the methods used to generate the data in Table 6 have not yet been calibrated against case histories. The shear strain and displacement data in Table 6 should be considered maxima because the method used estimates limiting or potential strain.

TABLE 6. CALCULATION OF VOLUMETRIC AND LIMITING SHEAR STRAIN ALONG WITH SETTLEMENT AND HORIZONTAL DISPLACEMENT FOR EACH GEOLOGIC MAP UNIT

map unit at surface	#	Volumetric strain (%)				Settlement (meters)				Shear strain (%)				Displacement (meters)			
		μ	med	σ	C	μ	med	σ	C	μ	med	σ	C	μ	med	σ	C
afbm	6	4.5	4.8	0.6	0.1	0.1	0.1	0.5	42.1	43.0	5.4	0.1	1.2	1.0	0.7	0.6	
alf	24	3.1	--	1.7	0.5	0.1	0.1	0.2	0.4	26.5	27.1	16.8	0.6	1.0	0.5	1.3	1.3
ac	2	2.7	2.7	0.9	0.3	0.2	0.2	0.1	0.8	26.8	26.8	9.0	0.3	1.9	1.9	1.5	0.8
Qhc	3	1.0	0.5	1.3	1.3	0.0	0.0	0.1	1.6	7.9	0.0	13.7	1.7	0.4	0.0	0.6	1.7
Qhfy	21	3.1	3.0	1.4	0.5	0.1	0.1	0.1	0.7	28.6	27.2	15.6	0.5	0.9	0.7	0.7	0.8
Qhly	28	2.7	2.9	1.6	0.6	0.1	0.1	0.1	1.0	24.9	24.2	17.7	0.7	1.1	0.8	1.2	1.1
Qhty	18	3.2	3.2	1.3	0.4	0.1	0.1	0.1	0.7	30.0	27.5	16.0	0.5	0.9	0.8	0.7	0.8
Qhfe	11	4.2	4.1	2.0	0.5	0.2	0.1	0.2	0.8	33.8	30.3	15.1	0.4	1.6	1.1	1.4	0.9
Qhf	183	1.4	0.8	1.7	1.2	0.0	0.0	0.1	2.0	11.7	0.6	16.3	1.4	0.3	0.0	0.8	2.3
Qhff	72	2.2	2.1	1.6	0.8	0.1	0.0	0.1	1.1	18.9	14.7	16.8	0.9	0.5	0.3	0.7	1.2
Qhl	87	2.4	2.6	1.8	0.7	0.1	0.0	0.1	1.1	21.7	20.9	17.9	0.8	0.6	0.4	0.7	1.1
Qht	4	2.3	2.3	1.5	0.7	0.2	0.2	0.1	0.8	20.1	19.3	15.4	0.8	1.6	1.5	1.5	0.9
Qf	6	1.2	1.3	0.8	0.7	0.0	0.0	0.0	1.2	5.3	6.1	4.8	0.9	0.1	0.0	0.1	1.5
Qt	1	0.9	--	--	--	0.1	-	-	-	1.0	--	--	--	0.2	-	-	-
Qpf	23	0.2	0.0	0.4	2.3	0.0	0.0	0.0	2.7	0.5	0.0	1.3	2.5	0.0	0.0	0.1	3.0
By representative deposit age for each boring																	
Artificial fill	6	3.7	4.6	2.2	0.6	0.2	0.1	0.2	0.4	33.4	43.6	21.4	0.6	1.4	0.9	2.0	0.4
Holocene	379	2.2	2.2	1.8	0.8	0.1	0.0	0.1	0.4	19.3	15.9	18.0	0.9	0.6	0.3	0.7	0.4
Late Pleistocene	110	1.4	0.8	1.6	1.1	0.1	0.0	0.1	0.5	11.8	1.0	15.8	1.3	0.6	0.0	1.1	0.6

See Table 1 for listing of names of geologic map units

“Predicted” volumetric strain is calculated and shown here using the Wu et al. (2004) approach. This method assumes nearly level ground and, based on comparison with case studies yields estimates that should be within a factor of two of future settlement.

See Table 1 for listing of names of geologic map units

“Limiting” shear strain is calculated and shown here using the preliminary correlations by Wu (2002). This method assumes nearly level ground and yields estimates that should be considered maxima

- number of borings; μ - mean; med - median; σ - standard deviation; C - coefficient of variation

Table 6 lists the geologic map units from youngest (top) to oldest (bottom). Inspection of the tables reveals that there is an inverse correlation between deposit age and estimated strain – generally, the younger the deposit the larger the estimated strain. The younger deposits (e.g. the late Holocene units Qhfy, Qhly, Qhty and Qhfe) are likely to be looser and thus more susceptible to liquefaction triggering and the subsequent deformation. Further, the maps in Figures 21 and 22 show that potential strain is greatest near the larger streams, where youthful, cohesionless sediment tends to be found.

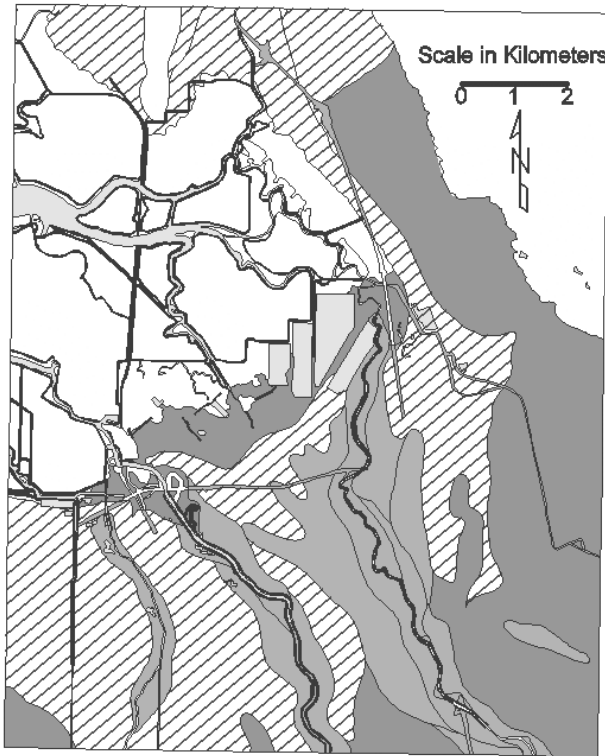
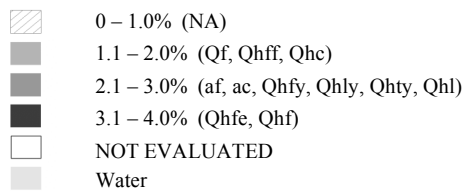


Figure 21. Liquefaction-induced vertical strain, Milpitas 7.5-minute quadrangle (strain calculated using Wu et al., 2004 method)



Work is still needed to calibrate the results of each method for calculating liquefaction-induced ground deformation against case histories. Several instances of historical ground failure have been recorded within the study area. It will be useful to review the literature describing actual ground failure events and, where possible, compare measured values of settlement and displacement with predicted and potential values.

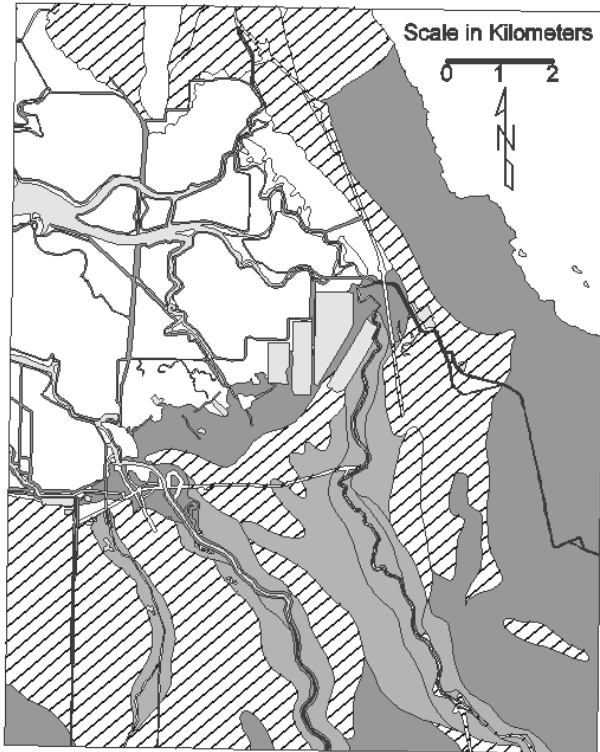
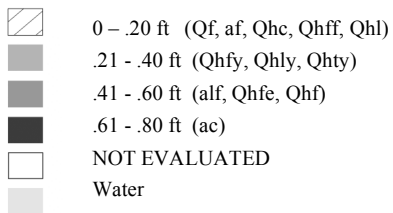


Figure 22. Liquefaction-induced ground settlement (ft), Milpitas 7.5-minute quadrangle, (settlement calculated using Wu et al., 2004 method)



Prediction of lateral spread deformations

Topography

The lateral spread study area is an approximately 26-square mile (67-square kilometer) area on the eastern side of the Santa Clara Valley (Figure 23). This area is much smaller than the area addressed using some of the other methods because of the large file sizes that are typical of terrain data. The northern part of the study area is bounded by the south shore of San Francisco Bay. Elevations in the study area range from sea level along the shore to a little over 40 feet above sea level on the northeast side of the study area. Natural slopes in the study area are very gentle except along stream banks and on various manmade features such as channel embankments, levees, road embankments and landfills. Most of the study area slopes less than one-percent to the north and northwest. A small area in the northeast corner of the study area slopes one- to three-percent to the west and southwest. Stream banks and some manmade features slope 20 percent or greater in a few areas.

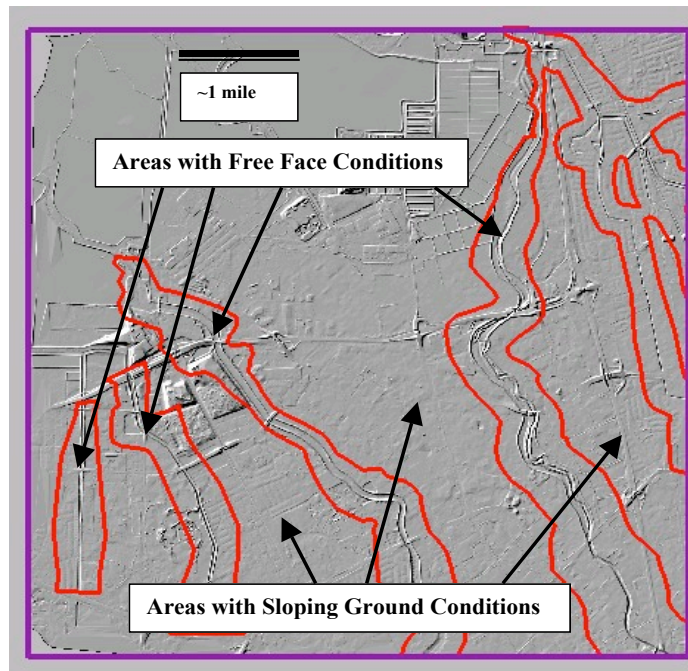


Figure 23. Lateral spread study area showing free face and sloping ground areas. Shaded relief image generated from photogrammetric breaklines and elevation points generated for orthophotographic rectification.

Coyote Creek and the Guadalupe River flow northwest across the alluvial plain to the San Francisco Bay. These streams are incised below the alluvial plain, which results in a free face condition above the stream bottom. The stream banks range from a few feet to more than 10 feet in height. Flood control levees are present along the top of the stream banks along both Coyote Creek and the Guadalupe River. There are also several smaller creeks and manmade drainage channels in the study area with sloping embankments that form free faces.

Topographic Parameters Needed for Displacement Calculations

Accurate topographic data is needed for regional horizontal displacement calculations using either the four- or six-parameter methods. Accurate measurements of slope gradient (S) and free face ratio (W) are required. Sensitivity analyses show that displacement calculations are sensitive to small changes in both slope gradient and free face ratio.

Slope Gradient Data

Figure 17 shows the sensitivity of slope gradient to horizontal displacement calculations. The plot shows that displacement calculations are affected by small changes in slope gradient on slopes that are less than about 2 percent. The sensitivity decreases as slopes become steeper than 2 percent. The sensitivity analysis shows that very accurate slope gradient data is needed to predict horizontal displacement on gentle slopes. Thus, slope gradient data used in this kind of analysis should be accurate to a fraction of a percent. Large-scale maps with two-foot contour intervals (or better) are needed for this level of precision. This data was not available in the study area, so more approximate slope gradients were derived from five-foot contours on the USGS topographic maps.

Free Face Ratio

Free face ratio is defined as the ratio in percent of the height of the free face divided by the horizontal distance from the top of the free face (Figure 16). Figure 17 shows the sensitivity of free face ratio to horizontal displacement calculations. The plot shows that displacement estimates are affected by small changes in free face ratio when the free face ratio is between 1 and 5 percent.

Accurate, up-to-date topographic data is needed to show the location of free faces such as stream banks and channel embankments. A common problem is that free faces along stream banks are often obscured by tree canopies and vegetation. These obscured areas may not be captured on photogrammetrically derived topographic maps with limited ground control or by remote sensing techniques that do not penetrate vegetation, such as interferometric radar surveys. Older topographic data may not show recent free face features such as artificial drainage channels or re-graded natural channels, both of which are present in the study area.

Evaluation of Topographic Data Sources

The topographic parameters needed for regional displacement analyses are best derived from Digital Elevation Models (DEMs) generated from large-scale maps with small contour intervals. In general, this information is becoming more readily available because many cities and counties are contracting for services that deliver detailed digital contour data. Often the contour files are large and not easily processed to DEMs by desktop computers, however, it is likely that digital terrain data will become more accessible as mapping technologies and terrain analysis software improves.

For this study, detailed digital contour data were not available so other sources of terrain data were investigated. The data sources investigated for this study included the following:

- 1) USGS 7.5-minute topographic map and digital elevation model (DEM)
- 2) Photogrammetric breaklines and elevation points generated for orthophoto rectification
- 3) Interferometric Radar DEM
- 4) LiDAR survey

The suitability of these topographic data for deriving slope gradient and free face ratio are discussed in the following sections.

USGS 7.5-Minute Topographic Map and Digital Elevation Model (DEM)

The USGS has generated DEM's from many of their 7.5-minute topographic quadrangles. We obtained the DEM of the Milpitas 7.5-minute quadrangle. The Milpitas quadrangle has a map scale of 1:24,000. The contour interval of the portion of the map that lies in the study area is five feet.

The 7.5-minute DEM's are created by a process that interpolates between the elevation contours on the 7.5-minute quadrangle maps. The 7.5-minute DEMs have a horizontal resolution of 10-meters and an estimated vertical accuracy within 7.5 meters. The vertical accuracy in gently sloping areas is likely considerably greater.

In the Milpitas quadrangle, the contours were photogrammetrically derived from 1948 aerial photography and therefore do not show terrain changes associated with human activities over the last few decades, such as construction of new drainage channels and modifications to natural channels.

A slope gradient map was made from the USGS DEM using a third-order, finite difference, center-weighted algorithm (Horn, 1981), however, the resulting map was inaccurate and showed an artificial, stepped topographic pattern in the study area. To correct this, the 5-foot contours were digitized from a scanned image of the 7.5-minute Milpitas quadrangle and DEM grid file was generated from the digitized contours. A slope gradient map was made from this DEM with a slope gradient resolution of 0.1-percent.

The following observations were made regarding the suitability of USGS topographic data for deriving topographic parameters for regional horizontal displacement mapping:

Slope Gradient – Slope gradient maps can be made from USGS topographic data; however, the slope gradient maps are less accurate than those that could be made from more detailed contour data. Because more detailed contour data was not available, the slope gradient map made from the USGS contours was used for the horizontal displacement calculation in this study.

Free Face Ratio - The USGS DEM did not consistently and accurately capture free faces in the study area such as stream banks along the Guadalupe River and Coyote Creek. Figure 24 shows an example of a poorly depicted free face along the Guadalupe River in the study area. It is likely that many of the free faces were obscured by vegetation or were too small to be accurately mapped by photogrammetric methods at 7.5-minute map scale. Also, some of the free faces may have been smoothed out by the DEM interpolation process. Also, the USGS contours do not show free faces created by manmade activities after the 1948 photography.

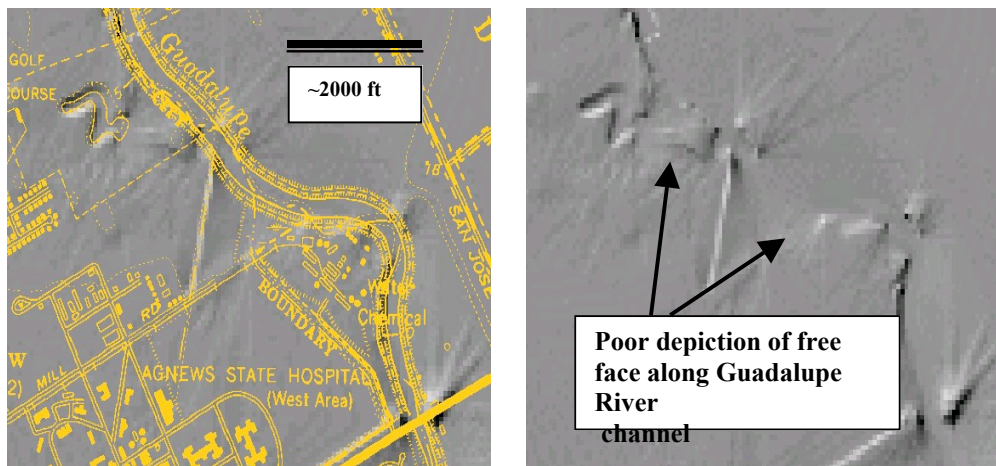


Figure 24. Shaded relief image from USGS DEM showing poor depiction of free face along the bank of the Guadalupe

Photogrammetric Breaklines and Elevation Points Generated for Orthophoto Rectification

Three-dimensional digital files of photogrammetrically-derived breaklines and approximate elevation points were obtained for an orthophotographic mapping project done in Santa Clara County by a commercial vendor. According to the vendor, the breaklines and elevation points were of sufficient accuracy to rectify orthophotos but not to generate accurate contours.

The following observations were made regarding the suitability of breakline and elevation point data for deriving topographic parameters for regional horizontal displacement mapping:

Slope Gradient – The elevation point data was not sufficiently accurate to generate accurate slope gradient maps. Shaded relief images of the data show numerous

topographic anomalies and cultural features that would introduce errors in the slope gradient maps.

Free Face Ratio – The breaklines accurately depict the tops and bottoms of the free faces along stream channels and artificial drainage channels in the study area. Prominent channels can be seen in the shaded relief image shown in Figure 25. The height of the free faces could be estimated from the elevation values of the breaklines.

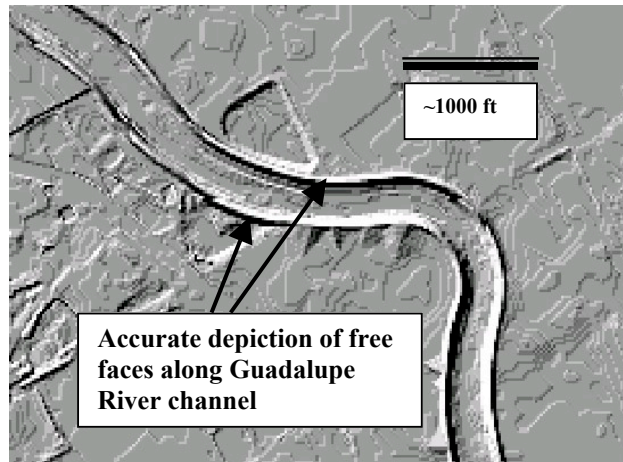


Figure 25. Shaded relief image made from photogrammetric breaklines and elevation points showing accurate depiction free faces along Coyote Creek and Guadalupe River

Interferometric Radar DEM

A DEM of the Milpitas quadrangle generated from airborne interferometric radar data was acquired from a commercial vendor. The radar data was acquired in 1998 and is therefore more up-to-date than the USGS DEM and shows terrain changes due to recent grading. The radar data was processed by the vendor to eliminate false topography from buildings, trees and other non-topographic features to approximate a “bald earth” condition. The radar DEM has a horizontal resolution of 5 meters and an estimated vertical accuracy of 1.5 meters.

The bald earth radar DEM was not suitable for deriving slope gradient and free face ratio. The following observations were made:

Slope Gradient - The bald earth radar DEM shows false undulations of topography in gently sloping areas, visible on a shaded relief image shown on Figure 26. The resulting slope gradient map shows slopes of several percent in areas where the true slope is less than one percent. Additional processing of the radar data by the vendor may be possible to remove these errors; however, this was not attempted for this study.

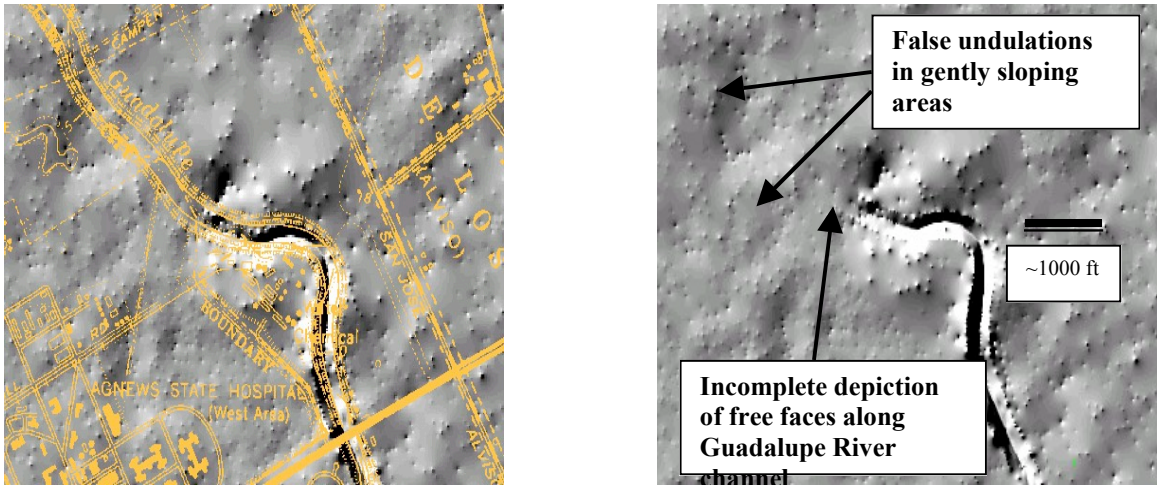


Figure 26. Shaded relief image from bald earth interferometric radar DEM showing false undulations in topography and poor depiction of free faces along bank of Guadalupe River

Free Face Ratio - The radar DEM does not consistently and accurately show free faces in the study area such as along the banks of Coyote Creek and the Guadalupe River. This is visible on the shaded relief images shown on Figure 26. The most likely reasons are that free faces along stream banks may have been obscured by tree canopies that could not be penetrated by the radar signals; alternatively, the stream geometry information may have been lost during the bald earth processing.

LiDAR Survey Data

LiDAR surveys are based on the detection of laser pulses that are reflected off the ground surface from an aircraft. Computer processing filters out reflections from trees and vegetation and retains reflections from the ground surface. DEM's can then be generated from the ground surface reflections.

We obtained LiDAR data of the study area from a commercial vendor. The survey data was delivered in more than 1,300 individual GIS files, each covering approximately 500 square feet, with three-dimensional data points spaced at about 4.5 feet. Each of the data files was about one megabyte and the entire data set exceeded one gigabyte. The vendor processed the data to eliminate false topography from buildings and other features to approximate a "bald earth" condition.

The LiDAR data accurately depicts many topographic features in the study area; however, the large number of files and the cumulative size of the data set were difficult to process on a personal computer. Only a small test area consisting of ten of the individual files was processed into a DEM for evaluation (Figure 27). The data would have been easier to use if the entire data set had been delivered as a DEM grid file by the vendor; however, this format was not specified in the contract.

The following observations were made regarding the suitability of LiDAR survey data for deriving topographic parameters for regional horizontal displacement mapping:

Slope Gradient - The “bald earth” processing of the LiDAR data done by the vendor was not successful in fully removing false topography from buildings. Figure 27 shows a shaded relief image with anomalous topographic features remaining at building locations. These anomalous features introduce errors in the slope gradient map. Additional processing of the LiDAR data by the vendor would be necessary to remove these anomalies.

Free Face Ratio - The LiDAR data appears to depict free faces well in the test area we evaluated (Figure 27). Additional testing of the data in areas with thick tree canopies is required to evaluate the depiction of free faces in heavily vegetated areas.

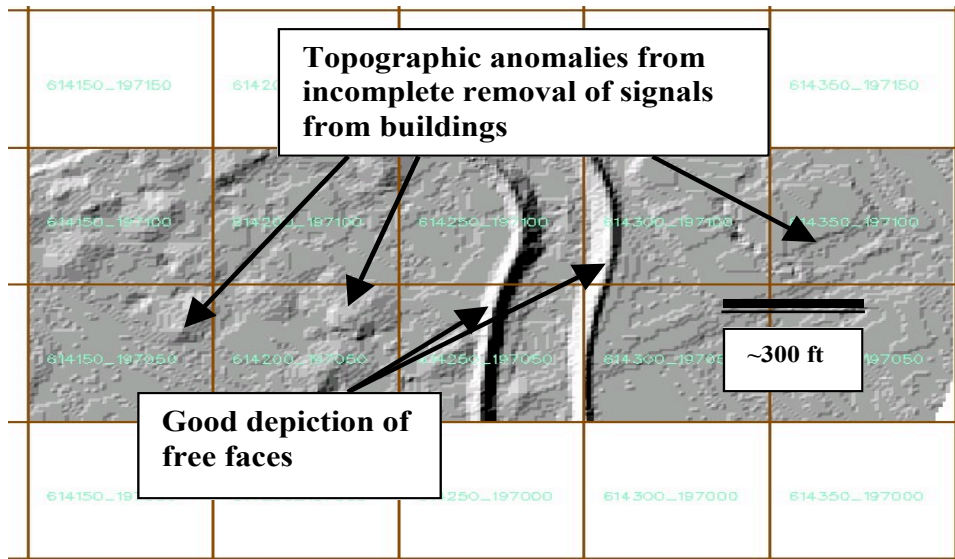


Figure 27. Shaded relief image of LiDAR test area showing topographic anomalies at building locations and accurate depiction of free face along bank of Guadalupe River

Calculation of Horizontal Displacement

To calculate horizontal displacement in the study area, a grid file was generated for each of the input parameters of the four-parameter model. A grid file consists of a two-dimensional array of cells with a value attached to each cell. A grid file header specifies the origin and spacing of the of the grid cells in the file. To process the input grid files, a script is written that performs a cell-by-cell calculation for each set of corresponding cells in the input grid files. In this case, the script is based on the equation for the Bardet et al. (1999) four-parameter model. The cell-by-cell grid calculation generates an output grid. In this case, the output grid shows the calculated horizontal displacement in the study area.

The following is a description of each of the input grids generated for the horizontal displacement calculation:

Moment Magnitude Grid

The moment magnitude grid used for this analysis is derived from the California statewide probabilistic seismic hazard evaluation that shows peak horizontal ground acceleration across the state having a 10% probability of exceedance in 50 years. The moment magnitude values in the study area are based on deaggregation of the seismic hazard model, which identifies the earthquake magnitude that contributes most to the seismic hazard at a particular location (predominant earthquake). The grid spacing derived from the statewide model is one kilometer. Moment magnitude values in the study area range from 6.4 to 7.9. An illustration of the moment magnitude grid is shown in Figure 28.

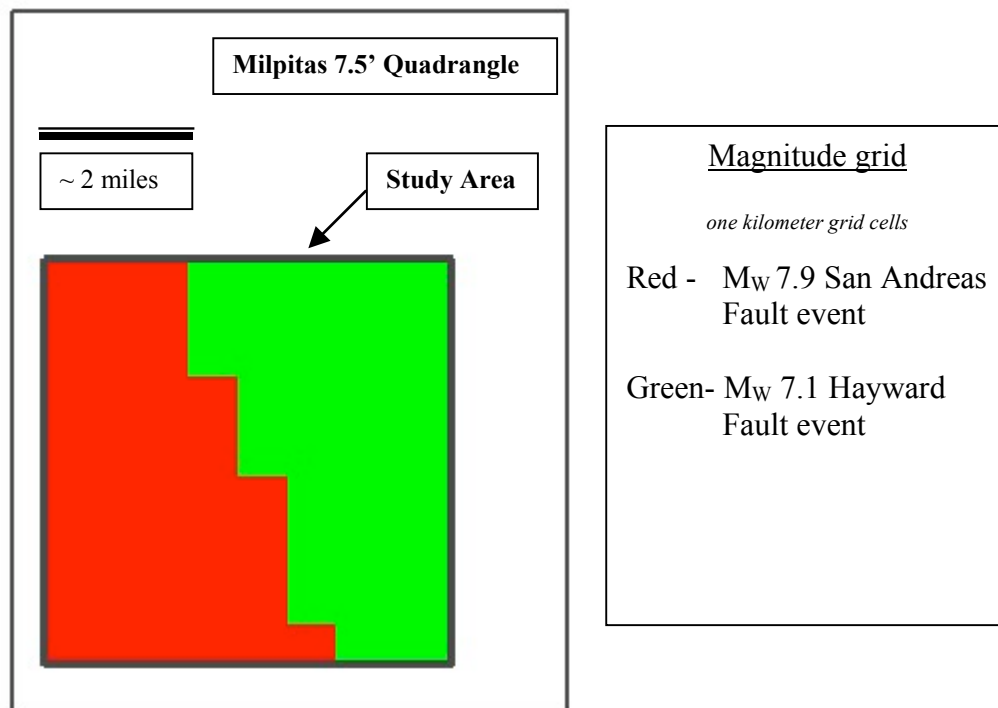


Figure 28. Moment magnitude grid

Distance from Seismic Source Grid

The grid showing distance from the seismic source also is derived from deaggregation of the California statewide probabilistic model (Petersen et al., 1996). The distance values of the grid cells are those that are associated with the earthquake that contributes most to the probabilistic ground motion. The distance values in the west and southwest portions of the map are associated with a large earthquake on the San Andreas Fault. The distance values in the east and northeast parts of the study area are dominated by large earthquakes on the Hayward Fault. The grid spacing is one kilometer.

Slope Gradient Grid (for ground slope condition)

The slope gradient (S) grid is based on the five-foot contours from the Milpitas 7.5-minute quadrangle. As discussed above, more detailed contour data is preferred and is becoming increasingly more available in digitized form from a variety city and county jurisdictions, however, it was not available for this study.

As noted above, we attempted to make a slope gradient map directly from the USGS DEM using a third-order, finite difference, center-weighted algorithm (Horn, 1981), however, the resulting map was inaccurate and showed an artificially stepped topographic pattern in the study area. We manually digitized and tagged the 5-foot contours from a scanned image of the 7.5-minute Milpitas quadrangle and built a triangulated irregular network (TIN) model from the digitized contours. We then converted the TIN model into a gridded DEM file. Finally, we made a slope gradient grid with a specified resolution of 0.1-percent using the Horn (1981) algorithm. Figure 29 shows the slope gradient grid. The slope gradient grid was only used in areas that had a free face ratio of less than 1 percent.

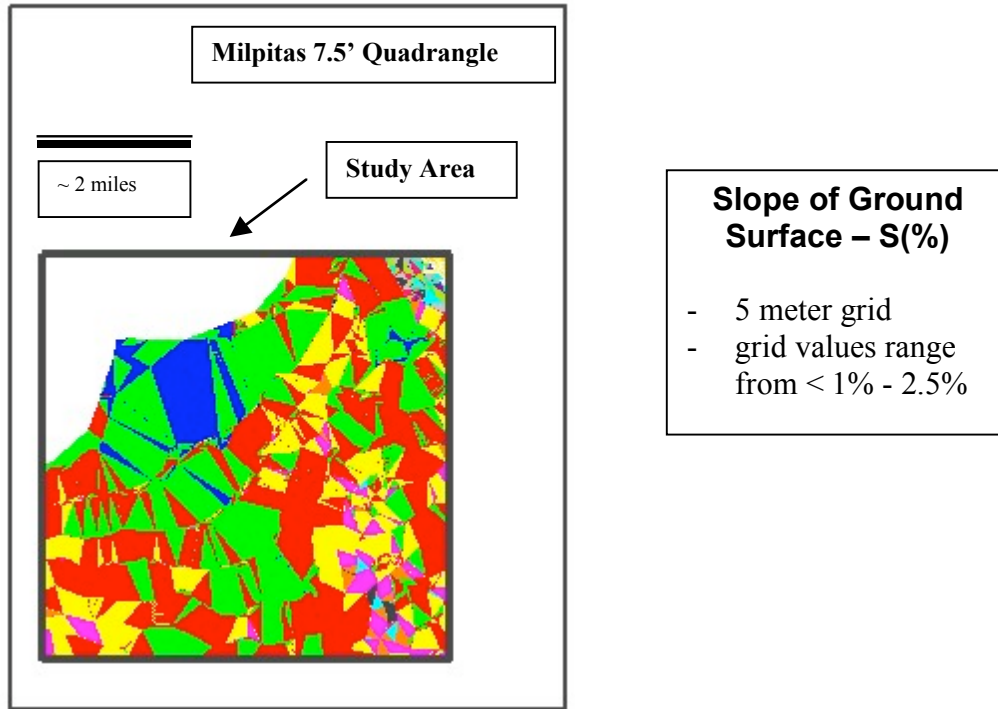


Figure 29. Slope gradient grid

Free Face Ratio Grid

The free face ratio grid was derived from photogrammetric breaklines generated by a commercial mapping vendor for rectifying an orthophoto project. Breaklines are three-dimensional linear features that are delineated to mark the location of sudden slope changes for generating digital terrain models. The files included accurate breaklines along the top and bottom of stream banks and stream channel slopes that form free faces. The heights of the free faces were estimated from the z-values of the breaklines. Digitized contours of equal free face ratio along the top of the stream banks and drainage channels were manually generated and drawn into the GIS – a very time consuming process. The free face grid was generated only in areas where the free face ratio is greater than one-percent. Figure 30 shows the free face ratio grid within this area.

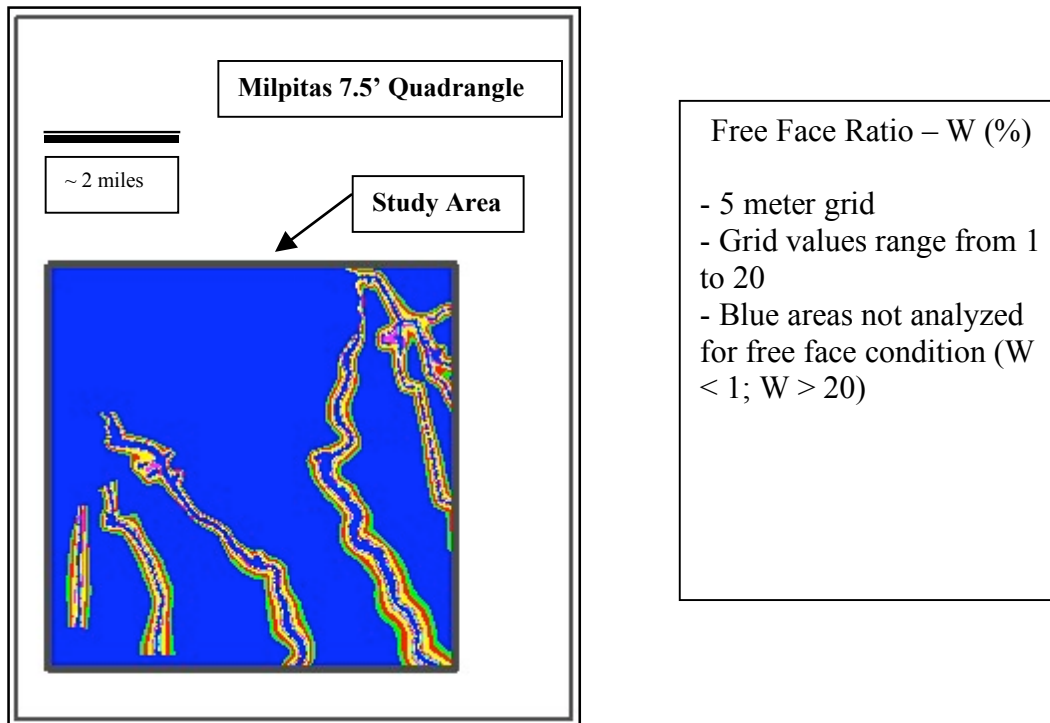


Figure 30. Free face ratio grid

T₁₅ Grid

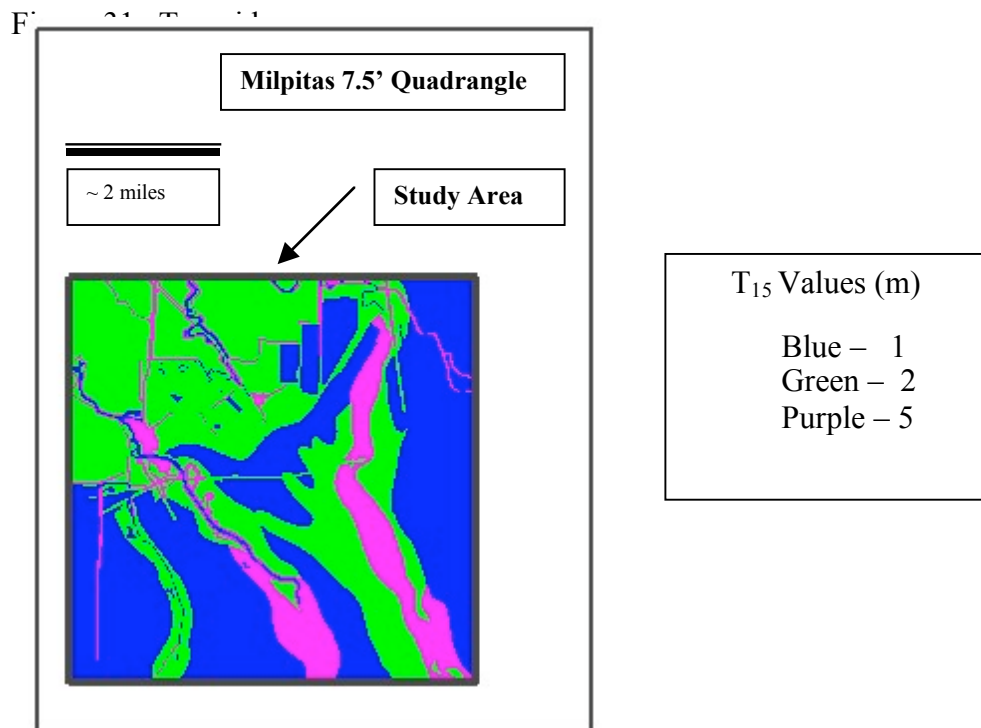
T_{15} is defined as the thickness in meters of saturated cohesionless soils with $N_{160} < 15$. The T_{15} grid was based on the statistical mean of T_{15} values calculated individually for each geologic unit for which borehole data were available. Geologic units were grouped based on similar mean T_{15} value. Geologic units having no borehole or well data were grouped based on similar lithology. The statistical analysis resulted in T_{15} values that ranged from zero to 5 meters. Various methods are available to assess which units should be grouped together to create the T_{15} grid. A contour map is not useful because it may not take into consideration the fact that borings are not all of uniform depth. Two borings may have similar T_{15} values, however a boring shallower than the required 20 m length may under represent the true value for T_{15} . A grid containing 4 zones with values of 0, 1, 2, and 5 m (Table 7) was made based upon the statistical mean of each grouping of geologic map units. The T_{15} values derived from the data were loaded into the digital geologic map database and a grid of the T_{15} values was generated. Figure 31 shows the T_{15} grid.

A preliminary geostatistical analysis indicates that the density of geotechnical data available for this project is not sufficient to make predictions in areas where there are not geotechnical data. Figure 32 shows a semivariogram that expresses this idea. The point at which the blue line curves, where its slope becomes horizontal, indicates a lag distance of about 900 m. This value is the maximum distance for which there is a relationship between adjacent borings (in the T_{15} parameter). This means that predictions should not

be made for areas that are more than 900 m from the nearest boring. The average distance between borings in this project's dataset is much more than 900 m. The conclusion from this analysis is that a greater density of borings is necessary to adequately characterize this area.

TABLE 7. SUMMARY OF GEOLOGIC MAP UNIT GROUPS FOR T₁₅

Thickness (m)	
0 m	Qt, Qa, Qpf
1 m	Qhf, Qhff, Qhl, Qht, Qf
2 m	af, Qhfy, Qhty, Qhfe, Qhbm
5 m	alf, ac, afbm, Qhc, Qhly



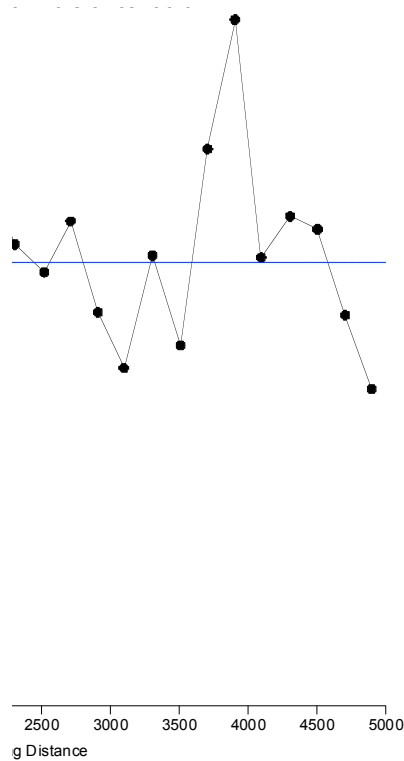


Figure 32. Semivariogram for T15 parameter

Horizontal Displacement Calculation

Two grids of horizontal displacement were generated, one for areas analyzed for ground slope conditions and one for areas analyzed for free face conditions.

Ground Slope Conditions

The areas analyzed for ground slope conditions are those areas that are far enough away from a free face to result in a free face ratio of less than one percent. This condition covers approximately 74 percent of the study area.

The results of the horizontal displacement calculation for areas analyzed for gentle slope conditions yielded displacement values that ranged from less than 1 centimeter to 84 centimeters. A breakdown of calculated horizontal displacements in the part of the study area that was analyzed for gentle slope conditions is shown in Table 8.

Table 8. Summary of horizontal displacements in the part of the study area that was analyzed for gentle slope conditions

Calculated horizontal displacement (meters)	Percent of study area analyzed for gentle slope conditions
0 – 0.1	62
0.1 – 0.2	27
0.2 – 0.3	8
0.3 – 0.4	2
> 0.4	1

The displacement grid for gentle slope conditions is displayed in Figure 33. Areas with calculated displacements greater than 0.3 meters, which make up about 3 percent of the area analyzed, are mostly on slopes in the northeast part of the area that are steeper than 1 percent or on manmade dike or embankment slopes. Areas sloping less than 1 percent generally have predicted displacements of less than 0.2 meters.

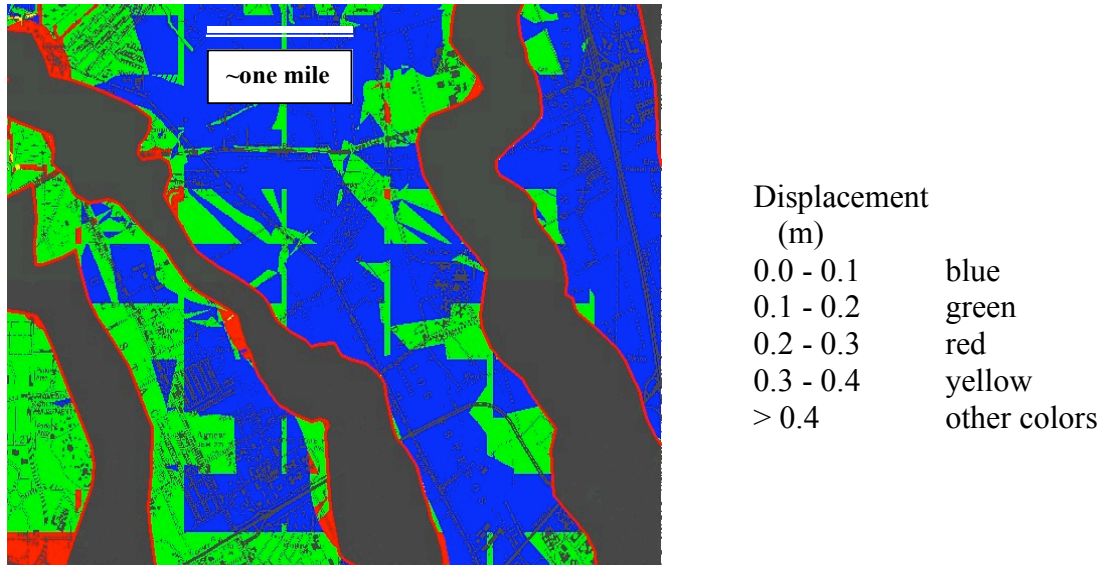


Figure 33. Horizontal displacement grid for areas analyzed for gentle slope conditions.

A marked rectilinear pattern can be seen in the displacement grid across much of the study area. The north-south and east-west lines match the edges of the one-kilometer magnitude and distance grids. The displacement values change at the boundaries of the grid cells due to changes in the magnitude (e.g. Figure 28) and distance input values.

Free Face Conditions

The areas analyzed for free face conditions are those areas with a free face ratio between 1 percent and 20 percent. About 21 percent of the study area meets these criteria. Areas that have a free face ratio greater than 20 are not analyzed because there is insufficient empirical data to support the model for areas close to large free faces.

The results of the horizontal displacement calculation for areas analyzed for free face conditions yielded displacement values that ranged from about 1 centimeter to 1.5 meters. A breakdown of calculated horizontal displacements in the part of the study area that was analyzed for free face conditions is shown in Table 9.

Table 9. Summary of horizontal displacements in the part of the study area that was analyzed for free face conditions.

Calculated horizontal displacement (meters)	Percent of study area analyzed for free face conditions
0.0 – 0.1	26
0.1 – 0.2	38
0.2 – 0.3	22
0.3 – 0.4	7
0.4 – 0.5	3.5
0.5 – 0.6	1.5
0.6 – 0.7	1
0.7 – 1.5	1

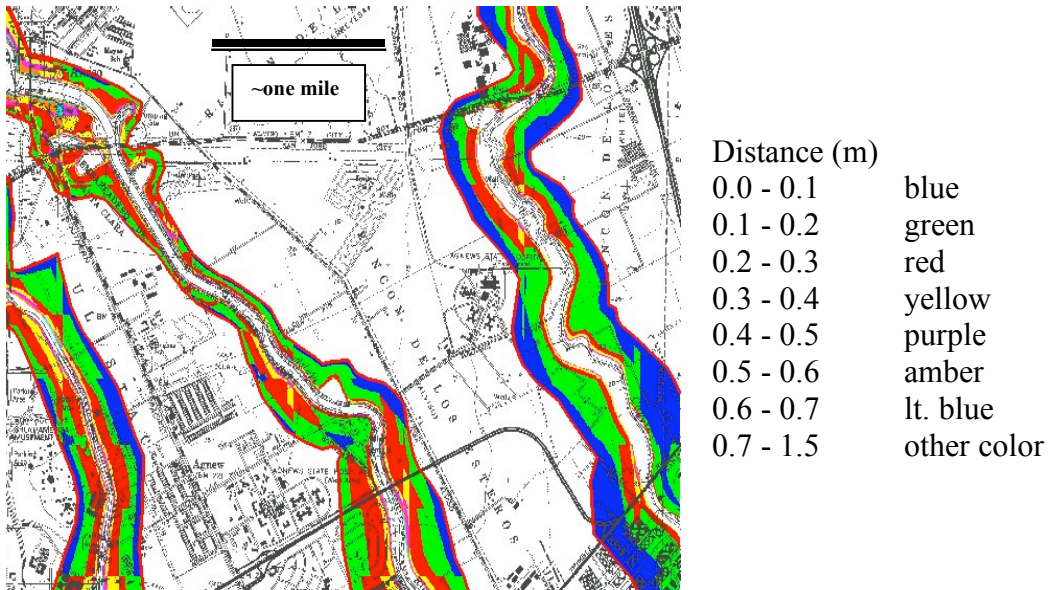


Figure 34. Horizontal displacement grid for areas analyzed for free face conditions.

The displacement grid for free face conditions is displayed in Figure 34. Areas with calculated displacements greater than 0.5 meters, which make up about 3.5 percent of the area analyzed, are almost all very close to free faces, generally where the free face ratio is greater than 5.

Liquefaction Potential Index approach

LPI has been calculated for all borings with saturated, loose granular deposits in the study area. Table 10 presents the values of LPI when aggregating the data so that borings are grouped by the Quaternary geologic map unit at the surface where the boring is advanced. Figure 35 shows LPI grouped in a different way - by the representative age of each boring. Because sediment becomes increasingly resistant to liquefying with age, LPI should decrease with increasing age, however calculated LPI values in this study do

not follow the expected trend. Deviation from expected results may be due to the fact that not all of the borings in this study reach the minimum required depth of 20 m, and/or that more data are needed. Alternatively, the variety in level of hazard across the study area may not be that large. Table 10 shows that many geologic map units have calculated mean or median LPI values in the range of 10 to 15. A value of 15 or more suggests that surface deformation should occur in a large earthquake, while values lower than 5 suggest that little surface deformation should occur (Toprak and Holzer, 2003). The Late Holocene deposits (Qhfy, Qhly, Qhty and Qhfe) all have relatively high values of LPI; this is in line with expectations. Figure 35 shows that LPI is not normally distributed but rather is likely a log-normal parameter. This figure also shows that LPI values for older deposits (Late Pleistocene) tend to be lower the values for younger (Holocene) deposits. For three reasons: (1) Table 10 did not show real differences in LPI values for different geologic map units, (2) the LPI parameter expresses only relative degree of hazard and not magnitudes of deformation, and (3) contouring of LPI values plotted on a map proved to be very problematic, it was decided not to further pursue producing maps using the LPI parameter as the basis for the mapping.

Table 10. LPI values for geologic map units

	# borings LPI	mean LPI value	median LPI value
afbm	6	12.2	7.6
alf	22	13.4	8.2
ac	2	20.7	20.7
Qhfy	20	12.4	10.8
Qhly	23	14.1	13.9
Qhty	17	13.5	12.2
Qhfe	11	19.9	16.6
Qhf	90	9.8	6.7
Qhff	55	11.2	8.1
Qhl	64	12.9	10.6
Qht	4	31.8	33.6
Qf	3	2.1	1.0
Qpf	3	5.8	5.0

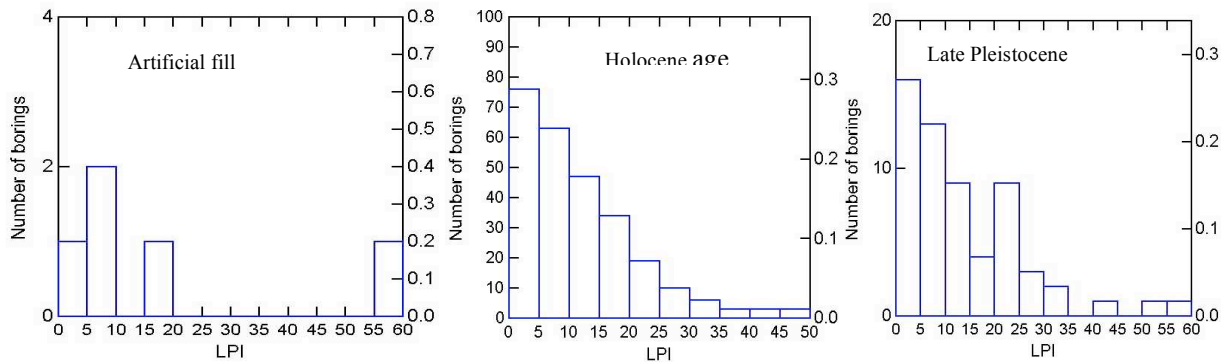


Figure 35. Liquefaction potential index calculated for borings aggregated to three ages of deposits: Artificial fill, Holocene and Late Pleistocene

CONCLUSIONS AND RECOMMENDATIONS

The methods used in this study allow for the production of viable regional liquefaction hazard maps that are based not just on the susceptibility of deposits to liquefaction but also on estimates of future surface deformation caused by liquefaction – if the geology in the area to be mapped is relatively simple and uniform. The most promising methods are those based on calculations of liquefaction-induced strain. Any of the methods have as their backbone detailed Quaternary geologic mapping and sufficient subsurface geotechnical information to adequately characterize geologic map units in three dimensions.

Based on Wu et al.'s (2004) study of case histories it appears that estimates of volumetric strain and settlement are likely to be within a factor of two for *site-specific studies* when using the approaches described above. Because the predictive relationships have been developed for nearly horizontal ground surfaces and for areas distant from free faces, predictions of shear strain and horizontal deformation entail greater levels of uncertainty than those for volumetric strain. Additionally, when the strain-based relationships are used to predict volumetric strain in areas that slope or that are near free faces, then the calculated strains should be considered minima.

With sufficient data to characterize the properties of each geologic map unit, maps of potential surface deformation can be developed by grouping units (and their respective map polygons) likely to experience similar quantities of deformation in future earthquakes. However, additional research into the characterization of geologic map units, possibly using geostatistics and analysis of variance and clustering techniques, and the identification of the appropriate parameters on which to base the mapping and grouping of map units is needed.

The existing empirical methods for predicting lateral spreads are probably accurate to within a factor of two for site-specific studies. However, when using these methods in regional mapping several problems arise. The four or six parameters used, depending on

which model is employed, are typically placed in GIS grid files. The different parameters can be mapped at different resolutions. For example, the seismological parameters (magnitude and distance to the fault) can not be mapped beyond grid cell sizes of about one square kilometer, but the topographic parameters (slope and free face ratio) can be mapped to much higher resolution depending on the size of the area to be mapped and the resources available for the topographic mapping. Remotely acquired terrain data, like LiDAR and Interferometric Radar, can be processed to “bald earth” terrain models. However, this is costly and the vendors that provided this project these data did not employ very successful methods in developing the bald earth models. For the T_{15} parameter to be well constrained, abundant geotechnical data should be used in areas where the geology is not simple and “layer cake”. Despite the relatively abundant available for this project, the characterization of T_{15} for the Santa Clara Valley was not well constrained.

The northern Santa Clara Valley may not be the best study area for a project like this one because of the highly variable nature of its Late Quaternary geology. This variability made it difficult to differentiate areas likely to experience large liquefaction-related deformation from areas with less hazard. Resolution of this problem might occur with the acquisition of additional geotechnical boring data. Clearly the data available for this project (more than 650 boring logs) was not sufficient to characterize the variability within or between geologic map units. Conversely, the difficulties in mapping degree of hazard may result from little difference in hazard across the study region or a relatively low level of liquefaction-related hazard in general across the area. A significant fraction of the sediment in the valley is likely too fine to liquefy.

The use of existing geotechnical boring data produced by a variety of practitioners under a range of conditions and using a variety of equipment and operators - and interpretations based on this data – leads one to be cautious about the level of certainty associated with predictions of deformation that are based on this information.

REFERENCES

- Bardet, Jean-Pierre, Mace, Nicholas, and Tobita, Tetsuo, 1999, Liquefaction-induced ground deformation and failure: University of Southern California, Department of Civil Engineering, Report to PEER/PG&E, Task 4A-Phase 1.
- Bardet, J. P., Tobita, T., Mace, N. and Hu, J., 2002, Regional Modeling of Liquefaction-Induced Ground Deformation: *Earthquake Spectra*, 18(1), p. 19-46.
- Bartlett S. F., and T. L. Youd., 1992, Empirical Analysis of Horizontal Ground Displacement Generated by Liquefaction-Induced Lateral Spreads: *Technical Report NCEER-92-0021*, National Center for Earthquake Engineering Research, Buffalo, NY.
- Clahan, K. B., Mattison, M. E., Rosinski, A. M., Bott, J. D. J., and Knudsen, K. L., 2002, Preliminary maps of (1) Pleistocene alluvial surface, (2) depth to historical high groundwater, and (3) thickness of Holocene alluvium – and their use in liquefaction hazard mapping, Santa Clara Valley and the East San Francisco Bay Plain, California *in* EOS, Transactions: American Geophysical Union, 83(47), p. F1312.
- Hamada, M., Yasuda, S., Isoyama, R. and Emoto, K., 1986, Study on liquefaction induced permanent ground displacements: Report of the Association for the Development of Earthquake Prediction in Japan, Tokyo.
- Ingebritsen and Jones, 1999
- Ishihara, K. and Yoshimine, M., 1992, Evaluation of settlements in sand deposits following liquefaction during earthquakes: *Soils and Foundations*, 32(1), p.173-188.
- Iwasaki, I., Tokida, K., Tatsuoka, F., Watanabe, S., Yasuda, S., and Sato, S., 1982, Microzonation for soil liquefaction potential using simplified methods: Proceedings, Third International Conference on Microzonation, Seattle, Washington, Volume 3, p. 1319-1330.
- Knudsen, K. L., Sowers, J. M., Witter, R. C., Wentworth, C. M. and Helley, E. J., 2000, Preliminary maps of Quaternary deposits and liquefaction susceptibility, nine-county San Francisco Bay Region, California: A digital database: U.S. Geological Survey Open-File Report 00-444.
- Knudsen, K. L., Rosinski, A. M., Wu, J., and Seed, R. B., 2004, Production of regional liquefaction-induced deformation maps: Proceedings, Eleventh International Conference on Soil Dynamics and Earthquake Engineering and Third International Conference on Earthquakes: Geotechnical Engineering, Berkeley, California, in press.
- Petersen, M.D., Bryant, W.A., Cramer, C.H., Cao, T., Reichle, M.S., Frankel, A.D., Lienkaemper, J.J., McCrory, P.A., and Schwartz, D.P., 1996, Probabilistic seismic hazard assessment of the State of California: California Department of Conservation, Division of Mines and Geology Open-File Report 96-08.
- Poland, 1984
- Rauch, A. F., 1997, EPOLLS: An empirical method for predicting surface displacement due to liquefaction –induced lateral spreading in earthquakes: Ph.D. dissertation, Virginia Polytechnic Institution, VA.
- Schmidt and Burgmann, 2002
- Seed, H. B. and Idriss, I. M., 1971, Simplified procedures for evaluating soil liquefaction potential: *Journal of Soil Mechanics and Foundations Division, ASCE*, 97(SM9), p.1249-1273.

- Seed, H.B. and Idriss, I.M., 1982, Ground motions and soil liquefaction during earthquakes: Monograph Series, Earthquake Engineering Research Institute, Berkeley, California, 134 p.
- Seed, H. B., Tokimatsu, K. and Harder, L., 1984, The influence of SPT procedures in evaluating soil liquefaction resistance: Earthquake Engineering Research Center, University of California, Berkeley, California, Report No. UCB/EERC-84-15.
- Seed, R. B., Cetin, K. O., Moss, R. E. S., Kammerer, A. M., Wu, J., Pestana, J. M. and Riemer, M. F., 2003, Recent advances in soil liquefaction engineering and seismic site response evaluation: International Conference and Symposium on Recent Advances in Geotechnical Earthquake Engineering and Soil Dynamics, paper SPL-2, San Diego, California, 71p.
- Seed, R.B., Dickenson, S.E., Riemer, M.F., Bray, J.D., Sitar, Nicholas, Mitchell, J.K., Idriss, I.M., Kayen, R.E., Kropp, Alan, Harder, L.F., and Power, M.S., 1990, Preliminary report on the principal geotechnical aspects of the October 17, 1989 Loma Prieta earthquake: Berkeley, University of California, Earthquake Engineering Research Center Report UCB/EERC 90/05, 137 p.
- Shamoto, Y., Zhang, J. M. and Sato, M., 1998, Methods for evaluating residual post-liquefaction ground settlement and horizontal displacement: Soils and Foundations, Special Issue 2, p. 69-83.
- Shamoto, Y., Sato M. and Zhang, J. M., 1996, Simplified estimation of earthquake-induced settlements in saturated sand deposits: Soils and Foundations, 369(1), p. 39-50.
- Tatsuoka, F., Sasaki, T. and Yamada, S., 1984, Settlement in saturated sand induced by cyclic undrained simple shear: Proceedings, Eighth World Conference on Earthquake Engineering, San Francisco, California, p. 95-102.
- Tokimatsu, K. and Seed, H. B., 1984, Simplified procedures of the evaluation of settlements in clean sands: University of California, Berkeley, California, Report Number UCB/GT-84/16,
- Tokimatsu, K. and Seed, H. B., 1987, Evaluation of settlement in sands due to earthquake shaking: Journal of Geotechnical Engineering, ASCE, 113(8), p. 861-878.
- Toprak, S., and Holzer, T. L., 2003, Liquefaction Potential Index: Field Assessment: Journal of Geotechnical and Geoenvironmental Engineering 129(4), p. 315-322.
- Wu, J., 2002, Liquefaction triggering and post liquefaction deformations of Monterey 0/30 Sand under uni-directional cyclic simple shear loading: Ph.D. dissertation, Department of Civil and Environmental Engineering, University of California, Berkeley, CA.
- Wu, J. and Seed, R. B., 2004, Estimation of Liquefaction-Induced ground settlement (case studies): Proceedings, Fifth International Conference on Case Histories in Geotechnical Engineering, Paper no. 3.09, New York, New York.
- Wu, J., Seed, R. B., and Pestana, J. M., 2004, Liquefaction triggering and post liquefaction deformations of Monterey 0/30 Sand under uni-directional cyclic simple shear loading: University of California, Berkeley, California, Geotechnical Engineering Research Report.
- Youd, T. L. and Jones, C. F., 1993, Liquefaction Hazard Maps for the Portland Quadrangle, Oregon in Earthquake Hazard Maps for the Portland Quadrangle, Multnomah and Washington Counties, Oregon, and Clark County, Washington,

- Portland, Oregon: Oregon Department of Geology and Mineral industries, GMS-79, p. 1-1 to 1-17.
- Youd, T. L., Hansen, C. M., and Bartlett, S. F., 2002, Revised MLR equations for prediction of lateral spread displacement: *Journal of Geotechnical and Geoenvironmental Engineering*, 128(12), p. 1007-1017.
- Youd, T. L. and Perkins, D. M., 1978, Mapping liquefaction-induced ground failure potential: *Journal of Geotechnical Engineering Division*, Volume 104, p. 433-446.
- Youd, T. L., Idriss, I. M., Andrus, R. D., Arango, I., Castro, G., Christian, J. T., Dobry, R., Finn, W. D. L., Harder, L. F., Hynes, M. E., Ishihara, K., Koester, J. P., Liao, S. C., Marcuson, W. F., Martin, G. R., Mitchell, J. K., Moriwaki, Y., Power, M. S., Robertson, P. K., Seed, R. B. and Stokoe, K. H., 2001, Liquefaction resistance of soils: Summary Report from the 1996 NCEER and 1998 NCEER/NSF Workshops on Evaluation of Liquefaction Resistance of Soils: *Journal of Geotechnical and Geoenvironmental Engineering*, 127(10), p. 817-833.
- Youd, T.L., Hanson, C.M., and Bartlett, S.F., 1999, Revised MLR equations for predicting lateral spread displacement in *Proceedings of the 7th U.S.-Japan Workshop on Earthquake Resistant Design of Lifeline Facilities and Countermeasures for Soil Liquefaction*: MCEER, edited by O'Rourke, T.D., Bardet, J.P., and Hamada, M., p 99-114.
- Youd, T.L., Hansen, C.M., and Bartlett, S.F., 2002, Revised MLR equations for prediction of lateral spread displacement: *Journal of Geotechnical and Geoenvironmental Engineering*, 128(12), p. 1007-1017.